

Multi-physics Model and Optimization of a Solenoid Valve

by

Kutlay Hanlı

A Dissertation Submitted to the
Graduate School of Sciences and Engineering
in Partial Fulfillment of the Requirements for
the Degree of

Master of Science

in

Mechanical Engineering



KOÇ ÜNİVERSİTESİ

December 19, 2022

Multi-physics Model and Optimization of a Solenoid Valve

Koç University

Graduate School of Sciences and Engineering

This is to certify that I have examined this copy of a master's thesis by

Kutlay Hanlı

and have found that it is complete and satisfactory in all respects,
and that any and all revisions required by the final
examining committee have been made.

Committee Members:

Assoc. Prof. Arif Karabeyoğlu (Advisor)

Prof. Metin Muradoğlu

Prof. Onur Tuncer

Date: _____

ABSTRACT

Multi-physics Model and Optimization of a Solenoid Valve

Kutlay Hanlı

Master of Science in Mechanical Engineering

December 19, 2022

There are several limitations when designing solenoid systems. With proper search space selection possible designs can be narrowed down lightest, fastest and most power efficient depending on the application. A method was developed starting from computing required coil design to overcome sealing forces, minimizing structural thicknesses to reduce weight and looking into the effect of manufacturing tolerances and clearances as a perturbation matrix. This was achieved by a multi-physics simulation where the magnetic circuit is modeled using magnetic reluctances of parts and clearances. The fluid flow was computed assuming ideal gas, 1D flow and adiabatic process.

ÖZETÇE

Solenoid Vana Çoklu-fizik Modeli ve Optimizasyonu

Kutlay Hanlı

Makine Mühendisliği, Yüksek Lisans

19 Aralık 2022

Solenoid sistemleri tasarlarken birçok kısıtlama vardır. Doğru tarama alanı ile olası tasarımlar en hafif, en hızlı ve en verimli olarak ayıklanabilir. Bobinin yenmesi gereken kuvvete göre bobin tasarlayarak başlayan, sonrasında ağırlığı azaltmak için yapısal kalınlıkları azaltan, üretim toleransları ve boşlukların etkisini hesaplayan bir model geliştirilmiştir. Bu model bir çoklu fizik modelidir, parça ve boşlukların relüktansını hesaplamaktadır. Akış hesaplamaları da ideal gaz, 1 boyutlu akış ve adyabatik süreç varsayımlarıyla hesaplanmıştır.

ACKNOWLEDGMENTS

I would like to express my gratitude to my supervisor Assoc. Prof. Arif Karabeyoğlu for their continuous support. I wish to show my appreciation to DeltaV engineers and close friends Murat Çetinkaya, Recep Ufuk and Utku Can Yıldız for their support in developing and testing our models in DeltaV facilities.

TABLE OF CONTENTS

| | |
|--|-------------|
| List of Tables | viii |
| List of Figures | ix |
| Abbreviations | xii |
| Chapter 1: Introduction | 1 |
| 1.1 Working Principles of Solenoid Valves | 1 |
| 1.1.1 Actuation Chamber Inlet and Outlet | 3 |
| 1.1.2 Actuation Chamber | 4 |
| 1.2 Problem Definition | 6 |
| Chapter 2: Magneto Motive Force | 12 |
| 2.1 Magnetic Flux | 12 |
| 2.1.1 Magnetic Reluctance | 12 |
| 2.1.2 $N \cdot I$ (Ampere Turns) | 17 |
| 2.2 Armature Surface Area | 17 |
| Chapter 3: Magnetic Model of a Solenoid Valve | 21 |
| Chapter 4: Dynamic Model of a Solenoid Valve | 26 |
| 4.1 Mechanical Model | 26 |
| 4.2 Electrical Model | 27 |
| 4.3 Simulation Meta Data | 29 |
| 4.4 Flow Model | 29 |
| 4.4.1 Armature Motion | 30 |
| 4.4.2 Electrical and Magnetic Circuit Simulation | 30 |

| | | |
|-------------------|---|-----------|
| 4.4.3 | Control Volume Changes | 31 |
| 4.4.4 | Gas Flows | 31 |
| Chapter 5: | Simulation | 34 |
| Chapter 6: | Optimization | 42 |
| 6.1 | Cost Functions and Constraints | 42 |
| 6.2 | Optimizing Coil Parameters | 43 |
| 6.3 | The Effect of Structural Elements Thickness | 45 |
| 6.4 | The Effect of Clearances and Tolerances | 46 |
| 6.5 | Sensitivity Analysis | 49 |
| 6.6 | \dot{m} vs ΔP Performance | 52 |
| Chapter 7: | Conclusion | 53 |
| | Bibliography | 54 |
| | Appendix A: | 55 |

LIST OF TABLES

| | | |
|-----|------------------------------|----|
| 6.1 | Sensitivity Matrix | 51 |
|-----|------------------------------|----|

LIST OF FIGURES

| | | |
|------|--|----|
| 1.1 | Pilot Operated Solenoid Valve Principles [Inst, 2019] | 3 |
| 1.2 | Valve States [Choi et al., 2021] | 4 |
| 1.3 | Main Plunger Force Balance | 5 |
| 1.4 | Pilot Plunger Force Balance | 5 |
| 1.5 | Bang-Bang pressure regulation for 50 Bar | 7 |
| 1.6 | Solenoid valve cycle | 7 |
| 1.7 | Main Plunger translation | 9 |
| 1.8 | Pressures | 10 |
| 2.1 | Magnetic flux through a simple bar | 13 |
| 2.2 | The structural schematic of the HSV [Zhao et al., 2017a] | 13 |
| 2.3 | Comparison between simulated and experimental results of the electromagnetic force [Zhao et al., 2017a] | 14 |
| 2.4 | Influence of the driving current on the electromagnetic force increment at different working air gaps [Zhao et al., 2017a] | 14 |
| 2.5 | Influence of driving current on total magnetic reluctance at different working air gaps [Zhao et al., 2017a] | 15 |
| 2.6 | The B-H curve of the iron core and armature. [Zhao et al., 2017a] | 16 |
| 2.7 | Influence of h on the electromagnetic force at different driving currents [Zhao et al., 2017a] (x axis is in 10mm) | 16 |
| 2.8 | Influence of h on the total magnetic reluctance at different driving currents [Zhao et al., 2017a] (x axis is in 10mm) | 17 |
| 2.9 | Electromagnetic force of different Ampere-turns [Yang et al., 2019] | 18 |
| 2.10 | Traditional micro high-speed digital valve [Yang et al., 2019] | 19 |
| 2.11 | Novel micro high-speed digital valve [Yang et al., 2019] | 20 |

| | | |
|------|---|----|
| 2.12 | Electromagnetic force for different arrangement [Yang et al., 2019] . . | 20 |
| 3.1 | Magnetic path shown on assembly | 21 |
| 3.2 | Detail view on vertical air gap between magnetic top and shell. . . . | 22 |
| 3.3 | Detail view on horizontal air gap between shell and magnetic bottom. | 23 |
| 3.4 | Detail view on horizontal air gap between magnetic bottom and ar- mature. | 24 |
| 3.5 | Detail view on vertical effective air gap between magnetic top and armature. | 24 |
| 4.1 | Armature Free Body Diagram | 26 |
| 4.2 | Schematic of electrical circuit. (left) Valve powered off. (right) Valve powered on. | 27 |
| 4.3 | (a) An RL circuit with a switch to turn current on and off. When in position 1, the battery, resistor, and inductor are in series and a current is established. In position 2, the battery is removed and the current eventually stops because of energy loss in the resistor. (b) A graph of current growth versus time when the switch is moved to position 1. (c) A graph of current decay when the switch is moved to position 2.[OpenStax, 2022] | 29 |
| 4.4 | Abstraction of valve volumes, and flow paths. | 30 |
| 5.1 | Electrical and magnetic circuit development over time. | 36 |
| 5.2 | Magnetic field strengths and magnetic flux densities reached during simulation. | 37 |
| 5.3 | All forces acting on the armature. | 37 |
| 5.4 | Forces acting on the armature excluding pressure forces. | 38 |
| 5.5 | Motion on the armature. | 38 |
| 5.6 | Mass flows to and from control volumes. | 39 |
| 5.7 | Pressures of control volumes and reservoirs. | 40 |
| 5.8 | Control volume pressure and temperature | 40 |

| | | |
|------|---|----|
| 5.9 | Change of the volumes | 41 |
| 5.10 | Change of the masses | 41 |
| 6.1 | Shortened simulation visualization. Simulation and driving voltage start at $t = 0$, and driving voltage is removed at the vertical black line. | 43 |
| 6.2 | Response times of various design options. Trade-offs between opening and closing times. | 44 |
| 6.3 | x axis represents the time it takes to flow 1 kg of gas during an oscillating valve operation (continuous opening and closing of the valve). | 45 |
| 6.4 | Results of simulation: Valve Weight and minimum flow per cycle . . . | 46 |
| 6.5 | Response times of various design options. Trade-offs between opening and closing times. | 47 |
| 6.6 | x axis represents the time it takes to flow 1 kg of gas during an oscillating valve operation (continuous opening and closing of the valve). | 47 |
| 6.7 | Results of simulation: Valve Weight and minimum flow per cycle . . . | 48 |
| 6.8 | The effect of clearances on valve opening and closing times. | 48 |
| 6.9 | The effect of clearances on valve weight. | 49 |
| 6.10 | The 3D model of the optimized valve. | 50 |
| 6.11 | \dot{m} vs ΔP for 50 bar inlet pressure and 273K temperature for nitrogen gas. | 52 |

ABBREVIATIONS

| | |
|-------------|----------------------------------|
| c_a | Axial clearance |
| c_r | Radial clearance |
| h_C | Coil height |
| h_{Cout} | Coil outer radius |
| D_w | Wire diameter |
| t_{cfr} | Coil former radial thickness |
| t_{cfa} | Coil former axial thickness |
| t_{mba} | Magnetic bottom axial thickness |
| t_{mta} | Magnetic top axial thickness |
| t_{shell} | Shell thickness |
| r_A | Armature radius |
| r_{cham} | Chamfer radius offset |
| h_{cham} | Chamfer height |
| PR | Solenoid packing ratio |
| CWCC | Coil wire current capacity |
| ERC | Electrical resistivity of copper |

Chapter 1

INTRODUCTION

Solenoid valves are used to control fluid flow in the industry. They operate by turning magnetic force into linear motion using a coil and a ferromagnetic armature. Typical industrial applications use 18-watt, 24 volt and 0.75 ampere coils to energize the armature. Furthermore, designs should take fluid compatibility into account. Solenoid valve designs for oxidizer must use oxygen compatible metals and sealing elements, whereas solenoid valve designs for petrochemical or other solvent chemical must prefer chemical compatible sealing elements.

The key design criteria for the safe operation of these valves are response time, flow rate and operating pressure. Precise control of these valves is critical in terms of the full duty cycle, i.e., fully opening the valve from a closed state and closing it from fully opened state. Precise control of these valves allows them to be used in cold gas thrusters and bang-bang gas regulators for aerospace applications.

In this study we iterated different assembly configurations to find the optimal balance between solenoid power, actuation chamber volume, pilot orifice and adjusting orifice to increase valve opening and closing speed. We first modeled the flow characteristics of the existing pilot operated solenoid valve by measuring valve opening and closing timings from solenoid power on and off signals.

1.1 Working Principles of Solenoid Valves

$$F = \frac{-V^2 \mu_r \mu_0}{8 \pi \gamma^2 l^2} \left(\frac{r_0}{r_\alpha} \right) \alpha e^{(-\frac{\alpha}{l} x)} \quad (1.1)$$

Eq. 1.1 is the equation for force applied on iron armature (plunger) where; V is the voltage applied, μ_r is permeability of the iron armature, μ_0 is permeability of air, γ is the resistance per unit length of the wire, r_0 is the inside radius of coil,

r_α is the center radius of coil, l is coil length, $\alpha = \ln(\mu_r)$ and x is the armature displacement. [Schimpf, 2013]

As seen in eq. 1.1 solenoid force F is inversely proportional to stroke (armature displacement). The focus of this study is to design an aerospace grade solenoid valve thus, power consumption is a design criterion to reduce. Therefore, a minimal stroke of 0.3 mm (about 0.01 in) was preferred. On the other hand, reducing stroke reduces flow restriction area thus limiting maximum flow rate.

$$A_c = h D \pi \quad (1.2)$$

The equation 1.2 shows the relation between stroke h , and flow restriction area A_c . Flow restriction area of plunger stroke is approximated by the side surface area of an upright cylinder. D represents the diameter of the orifice. Ideally flow should be restricted at the orifice thus the orifice surface area should be smaller than A_c . The orifice surface area is calculated using the eq. 1.3.

$$A_o = \frac{D^2}{4} \pi \quad (1.3)$$

To restrict flow at the orifice the following condition must be met:

$$\begin{aligned} A_c &> A_o \\ h D \pi &> \frac{D^2}{4} \pi \\ h &> \frac{D}{4} \end{aligned} \quad (1.4)$$

Solenoid armature stroke must be greater than one fourth of orifice diameter as seen above. Design of orifice diameter must satisfy solenoid force balance and pressure balance.

$$\dot{m} = C_d \frac{A P_t}{\sqrt{T_t}} \sqrt{\frac{\gamma}{R}} M \left(1 + \frac{\gamma - 1}{2} M^2 \right)^{-\frac{\gamma + 1}{2(\gamma - 1)}} \quad (1.5)$$

Above is the equation for mass flow rate for an ideal compressible gas where; \dot{m} is the mass flow rate, A is the area of flow restricting surface, P_t is the upstream gas pressure, T_t is the upstream gas temperature, γ is the specific heat ratio, R is the gas constant, M is the Mach Number of the flow. Upstream pressure and temperature are dependent variables because the solenoid valve must operate in different regimes.

Specific heat ratio and gas constant can only be controlled by restricting fluid type. For the two reasons above mass flow rate requirements are met by controlling the only independent variable flow restriction area.

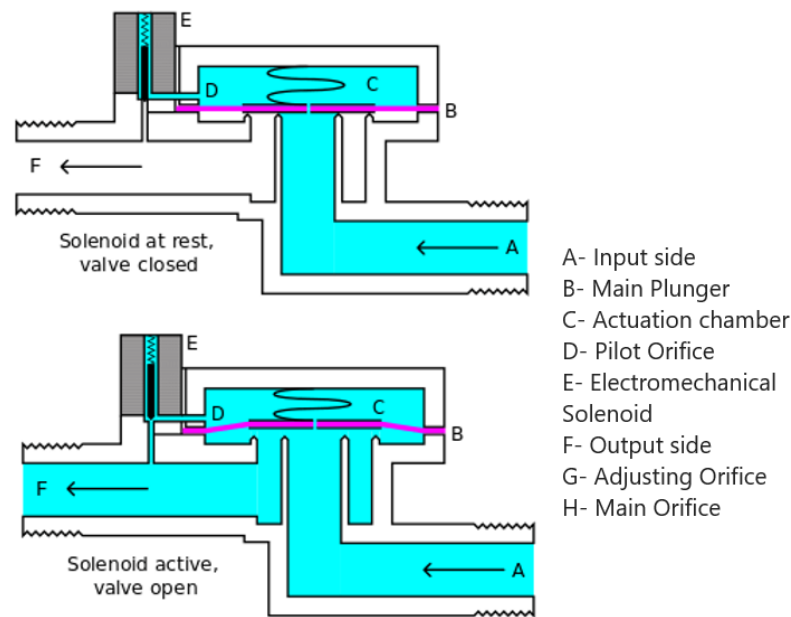


Figure 1.1: Pilot Operated Solenoid Valve Principles [Inst, 2019]

1.1.1 Actuation Chamber Inlet and Outlet

There are two flow restriction surfaces that dictate how the valve operates: pilot orifice (D) and adjusting orifice (G). Pilot orifice acts like the orifice of a single stage solenoid valve. Surface area of pilot orifice dictates how fast the actuation chamber is discharged. The designer should find a balance between pilot orifice area, solenoid power required to actuate the solenoid and adjusting orifice area.

The adjusting orifice area determines how fast the upstream fluid fills actuation chamber. If the adjusting orifice area is bigger than the pilot orifice area, the pilot operated solenoid valve will require a higher pressure differential to operate. For aerospace applications a low-pressure differential is preferred; thus, adjusting orifice area is a critical design parameter.

1.1.2 Actuation Chamber

Actuation chamber volume is critical for high-speed high flow rate pilot operated solenoid valves and dictates how much gas needs to be discharged from or filled into the actuation chamber to push the main plunger. Ideally, a negligible actuation chamber volume is desirable. Unfortunately, the range of motion of the pilot and the main plunger and the volume occupied by compression springs in the assembly only slightly increases actuation chamber volume which, limits how fast the main orifice of the pilot operated solenoid valve can open and close.

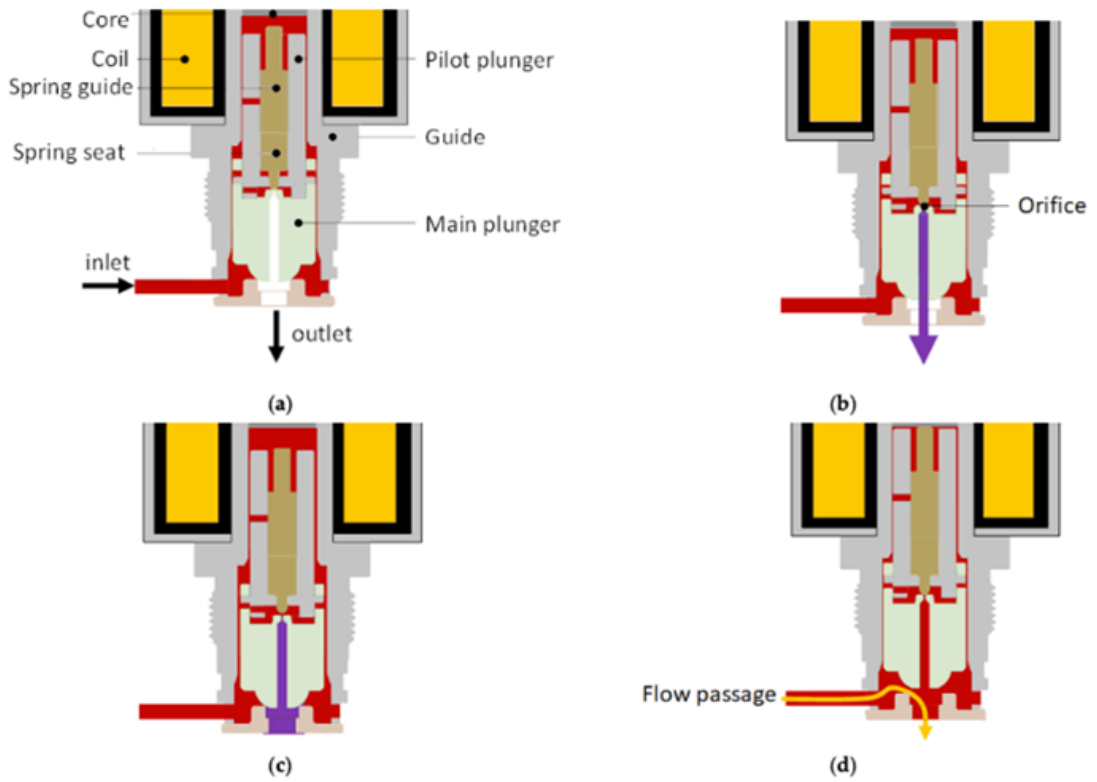


Figure 2. Principle of the pilot-operated solenoid valve: (a) initial state; (b) application of an electric voltage; (c) pressure equilibrium state; (d) opening of the flow passage.

Figure 1.2: Valve States [Choi et al., 2021]

As seen in the figure above valve opening, is divided into 3 steps. In this design the main plunger is PEAK plastic and is the main sealing material. The outlet body, the pilot plunger, and the plunger body are 304 stainless steel for oxygen compatibil-

ity. The main plunger force balance is presented below where F_s is the compression spring force, F_{ac} , F_{ups} and F_{dps} are the forces applied by the actuation chamber and the upstream pipe section and downstream pipe section pressure respectively.

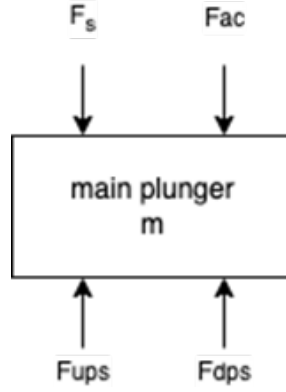


Figure 1.3: Main Plunger Force Balance

The pilot plunger force balance is presented below where F_s is the compression spring force, F_{em} is the solenoid electromagnetic force, F_{ac} , and F_{dps} are the forces applied by the actuation chamber and the downstream pipe section pressure respectively.

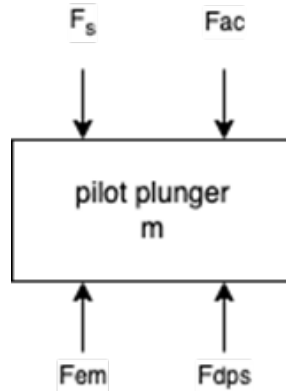


Figure 1.4: Pilot Plunger Force Balance

In the initial state (a) the actuation chamber pressure is equal to the upstream pipe section pressure and the downstream pipe pressure is lower than the upstream pipe section pressure. Net F forces the pilot plunger to press against the main plunger and seals the pilot orifice. In state b, the pilot is pulled by F_{em} overcoming

the spring and the pressure forces on the pilot plunger. The pilot orifice is opened and the fluid in actuation chamber start to discharge to the downstream pipe section. In state c, the increase in downstream pipe section pressure and the decrease in the actuation chamber pressure are observed. However, for the main plunger to move the actuation chamber pressure must fall below a critical threshold. In addition to the fluid discharge, fluid flows from upstream pipe section to actuation chamber through the adjusting orifice and pressurizes the actuation chamber. For the actuation chamber pressure to fall below the critical limit, the adjusting orifice mass flow rate must be smaller than the pilot orifice mass flow rate. In state (d), the actuation chamber pressure fell below the critical threshold and main plunger retracted. This opens the main orifice and high flow rate is achieved. The upstream pipe section pressure starts to tip off at this point to a level determined by the mass flow rate. The downstream pipe section pressure approaches to upstream pipe section pressure. Pressure difference between the upstream and the downstream pipe sections are determined by the mass flow rate.

1.2 Problem Definition

Pilot operated solenoid valves are used for bang-bang regulators and reaction control thrusters in aerospace applications. Valve weight, reaction time and flow rates are critical performance parameters. Due to valve reaction time delays the actual gas flow can exceed desired mass flow and reduce the control authority over the system.

This phenomenon can be observed in hybrid rocket propulsion and pressurization systems. In fig. 1.5, a 20L He tank was pressurized to 240 bars and denoted as source tank. A 100 L liquid oxygen tank is filled with a small ullage of He remaining. At $t = 53s$ the test starts as the main propulsion valve opens and the bang-bang regulator tries to regulate the pressure in the lox tank.

In fig. 1.5 the system initially shoots up almost 40% to 70 bars and undershoots down to 10%, 45 bars. This overshoot and undershoots happen because the valve opening and closing times can not react fast enough to the fluid discharge from downstream tank. As the ΔP reduced, the mass flow per cycle also reduced and

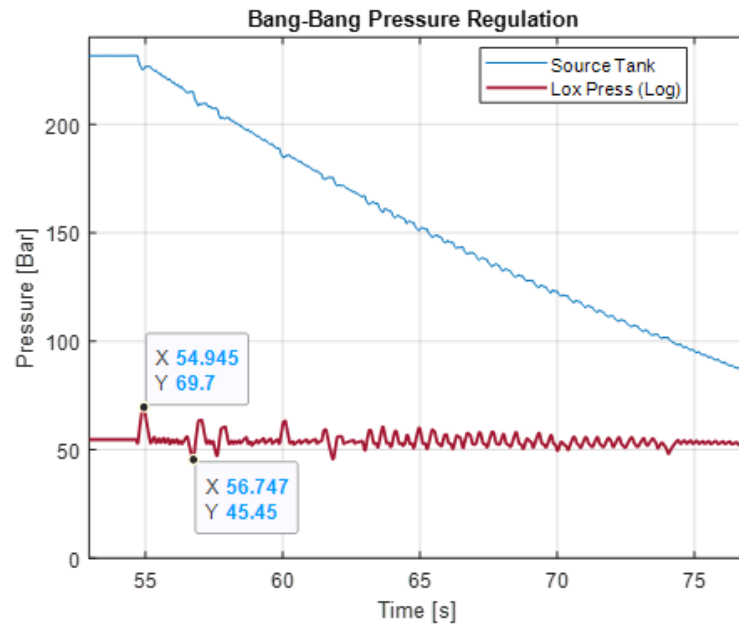


Figure 1.5: Bang-Bang pressure regulation for 50 Bar

the control authority was improved by the end of the test. As the lox discharges from the tank, the ullage volume increases. This increase in volume also dampens the effect of incoming gas on lox tank pressure.

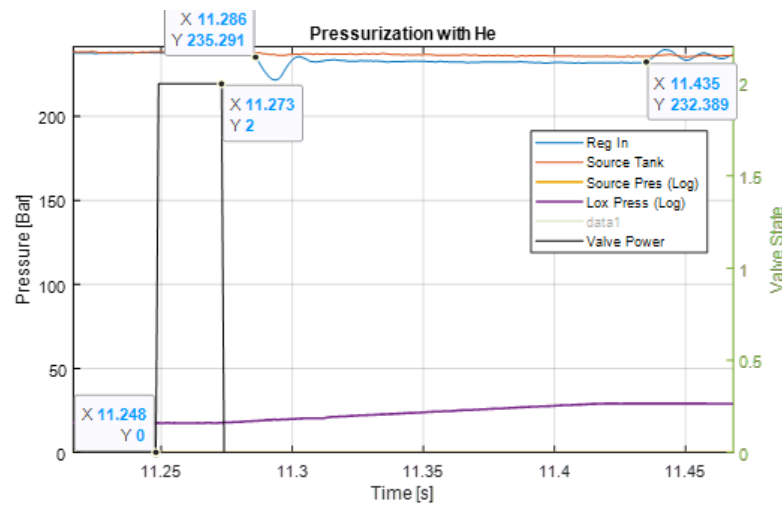


Figure 1.6: Solenoid valve cycle

The fig. 1.6 is focused on a single cycle of this solenoid valve. It is observed that the valve opens in $38ms$ after power on, the valve closes after $162ms$ after power off

and the total flow duration on $149ms$. Notice that the signal start and end points does not coincide with flow start or ending points. The signal duration of $25ms$ came up after rigorous testing. The goal of this paper is to build a multi-physic model to better understand the valve reaction time and optimize designs for specific applications.

Our initial theory was that the reason for poor response time was caused by the pressure balance in valve control volumes. In order to test it out we developed a computational model that assumed that there were no delay between valve power signal and pilot orifice translation. We than improved the valve design by resizing the control volumes and flow paths between these volumes.

Our model is constructed to observe the performance of the design under steady upstream and downstream pressure. It is assumed that there is an infinite upstream and downstream reservoir. The upstream reservoir pressure is set to $400Bar$, and the downstream reservoir pressure is set to $1Bar$. The pilot operated solenoid valve is connected to the upstream and the downstream reservoirs via the upstream pipe section and the downstream pipe section respectively. These pipe sections are critical for modeling because they simulate the plumbing the end user would use. Both pipe sections have a $15mm$, $\sim 0.6inch$, inside diameter and have a length of $250mm$, $\sim 9.85inches$. Upstream pipe section inlet surface area is restricted by the pipe diameter itself and is equal to $176.7mm^2$, $\sim 0.27squareinches$. The downstream pipe section is modeled to have a nozzle that discharges gas to the downstream reservoir to emulate other flow restricting components in plumbing. Nozzle orifice diameter is selected as $9mm$ and the area is $63.6mm^2$, $\sim 0.1squareinches$.

In the initial state upstream reservoir, upstream pipe section and the actuation chamber are at 400 Bars and 273 K. The downstream pipe section and the downstream reservoir are at 1 Bar and 273 K. A full simulation cycle is first opening the valve and obtaining steady mass flow then, closing the valve and waiting for the system to get back to equilibrium. At $t(0)ms$, the pilot plunger is retracted completely and at $t(3)ms$ the pilot plunger seals the pilot orifice. The total simulation time is $6ms$ and time step for the simulation is $1\mu s$.

Nitrogen gas is selected as the working fluid in this model. Mass flow rates for

the upstream pipe section inlet, the adjusting orifice, the pilot orifice, the main orifice and the downstream pipe section nozzle are computed using the equation for mass flow rate of ideal gases. First, Mach number is computed and limited to 1 since if the flow is choked in a converging nozzle, it cannot accelerate further than Mach 1. The total gas intake and releases for all control volumes are computed individually and put through a polytropic process. For this study the polytropic index is taken as 1.1 assuming that high velocity flow causes effective heat transfer with the valve body. Gas flowing through control volumes creates pressure changes that result in a change in net force applied on the main plunger. The main plunger acceleration is computed using this net force. The plunger position for next iteration is computed and another polytropic process is applied on the actuation chamber, with the expansion or contraction in volume by the main plunger movement.

In the chapter *Dynamic Model of a Solenoid Valve* we explain how our kinematics and flow model is constructed in detail.

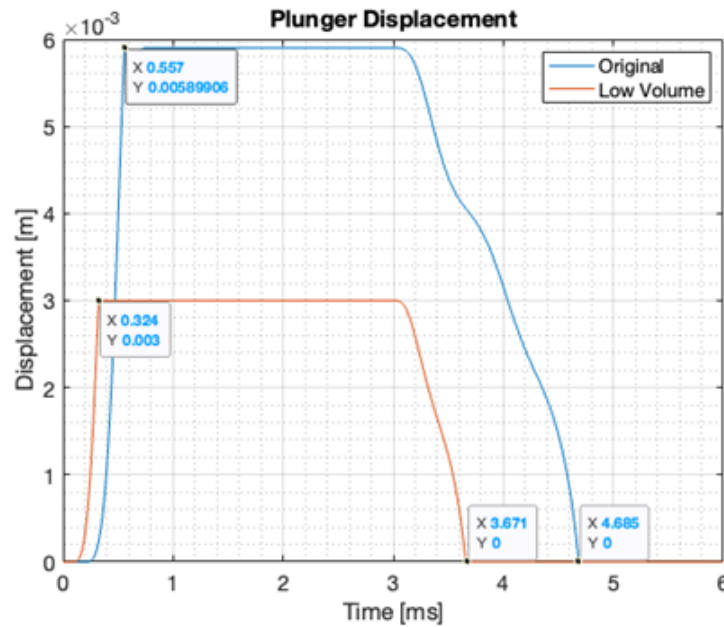


Figure 1.7: Main Plunger translation

Reducing actuation chamber volume reduces main plunger response time. Original design closed actuation chamber volume is 3,675 mm³ and the open actuation

chamber volume is 2,198 mm³. The new design has the following actuation chamber volumes for closed and open state respectively 1722 mm³ and 1037 mm³. The closed volume is reduced by 53% and the opened volume is reduced by 52%. The main plunger stroke was also reduced to 3 mm from 5.9 mm to facilitate the reduction in volume. The main plunger requires to travel a shorter distance thus opening and closing take less time. The pilot and the main orifice dimensions were kept the same to isolate the effect of volume change in pilot operated solenoid valve response time.

In the fig. 1.7 above pilot orifice is opened at $t(0)$ and closed at $t(3)$, (t in ms). As seen in the figure, low volume design responded faster to pilot orifice opening. Original design fully opened in 0.557ms and closed shut in 1.684ms. The low volume design on however opened fully in 0.322ms and closed shut in 0.665ms. Valve opening time reduced by 42% and closing time is reduced by 60%. This reduction in response time is due to faster settling time for the actuation chamber pressure.

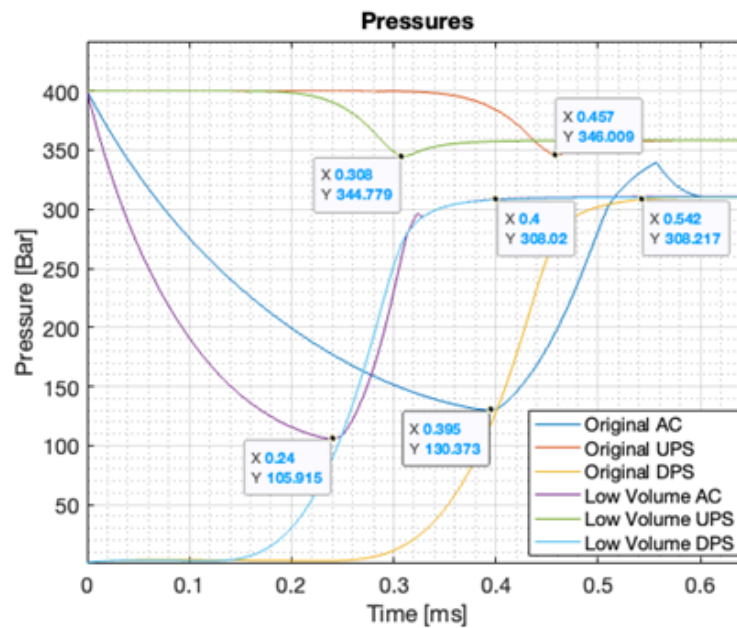


Figure 1.8: Pressures

Fig. 1.8 presents pressures at the opening phase of the pilot operated solenoid valve. In the original design, it takes 0.3ms for the action chamber pressure to drop to its minimum. In the low volume design, it only takes 0.24ms. The maximum force

difference between F_{ac} and F_{ups} is applied at this moment where the main plunger has the top acceleration to open. The maximum flow rate from the upstream pipe section to the downstream pipe section is achieved at the dipping point (downward spike) of the upstream pipe section pressure. In the original design, it takes 0.457ms to reach the maximum flow rate. In the low volume design, it takes 0.308ms to reach the maximum flow rate.

Our simulation showed that the initial hypothesis that the delay in valve response time is driven by the pressure balance between control volumes was wrong. To better analyze valve dynamics a multi-physics model should be developed. Our pilot operated valve simulation also showed that there is an order of magnitude difference between simulated main plunger responsiveness and real life responsiveness caused by electromagnetism. For these reasons the multi-physics model will be constructed for a direct acting solenoid valve.

Chapter 2

MAGNETO MOTIVE FORCE

Magneto motive force is the force that allows solenoid valves to open using the linear motion of an armature. Magneto motive force is a function of magnetic flux ϕ , surface area perpendicular to the magnetic flux acting on armature S_2 and magnetic reluctance of vacuum or material filling range of linear motion μ_0 .

$$F_{mag} = \frac{1 \cdot \phi^2}{2 \cdot \mu_0 \cdot S_2} \quad (2.1)$$

2.1 Magnetic Flux

Magnetic flux through the magnetic circuit of a solenoid valve is a function of coil turns N , current through the coil I , and total magnetic reluctance of the magnetic circuit R_{total} .

$$\phi = \frac{N \cdot I}{R_{total}} \quad (2.2)$$

N is constrained by the geometry of the valve, there is a limit on how many turns one can add for a given cross sectional area. I is constrained by the wire current carrying capacity. In further sections we will analyze the effect of wire diameter and valve geometry on magnetic flux and magneto motive force.

2.1.1 Magnetic Reluctance

Magnetic reluctance R of a simple 430F stainless steel block can be computed as:

$$R = \frac{l}{\mu_0 \mu_r A} \quad (2.3)$$

where l is length of the magnetic path in meters, μ_0 is permeability of free space (vacuum) $4\pi \cdot 10^{-7} H/m$, μ_r is relative permeability of a magnetic material (850 for 430F SS) and A is the cross sectional area in m^2 . [Zhao et al., 2017a] Zhao et al.

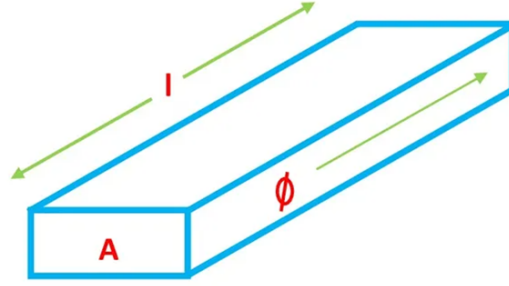


Figure 2.1: Magnetic flux through a simple bar

studied the effect of structural parameters of a solenoid system with the model in fig. 2.2.

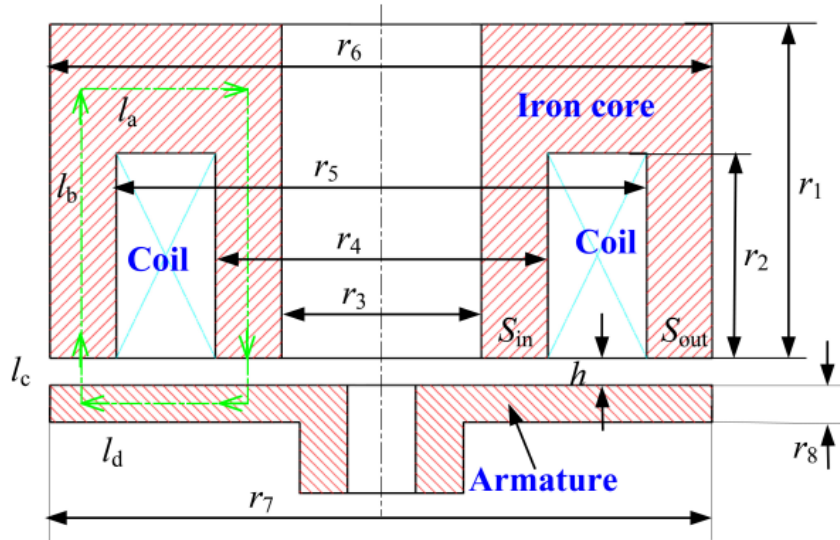


Figure 2.2: The structural schematic of the HSV [Zhao et al., 2017a]

Zhao et al. computed the total magnetic reluctance through the green arrows, magnetic circuit path, and computed the magnetic flux and magneto motive force. Researchers validated their static electromagnetic force model by running experiments on a test bench where they fixed the armature and the force sensor at one end and placed the iron core free on the other end 2.3. They present the effects of driving current on electromagnetic energy conversion in fig.

2.4.

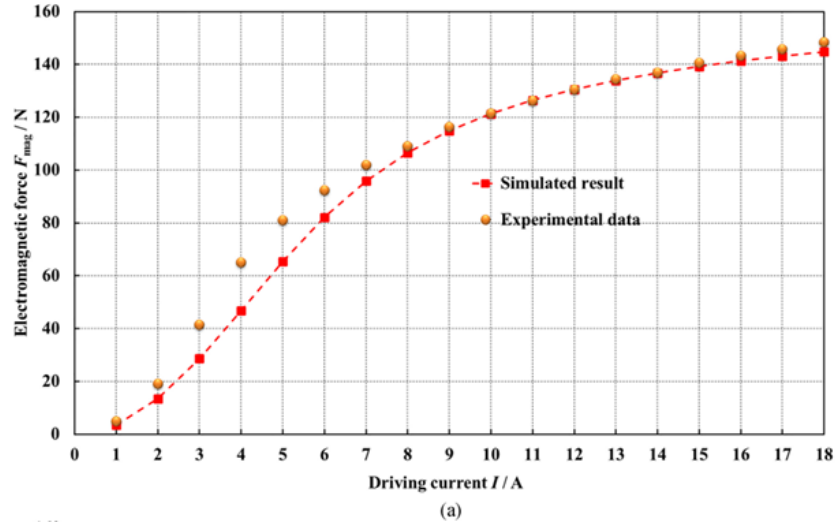


Figure 2.3: Comparison between simulated and experimental results of the electromagnetic force [Zhao et al., 2017a]

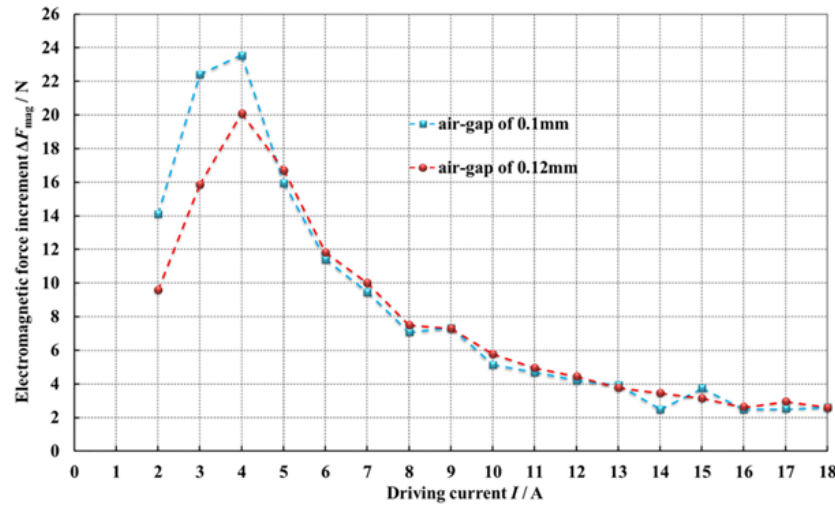


Figure 2.4: Influence of the driving current on the electromagnetic force increment at different working air gaps [Zhao et al., 2017a]

“When I increases from $1A$ to $18A$, the electromagnetic force first increases rapidly, $\partial F / \partial I$ reaches a maximum value at a driving current of $4A$, and then decreases. When $I < 4A$, with increasing I , the increase of the electromagnetic force at the air gap of $0.1mm$ always greater than that at the air gap of $0.12mm$. When $I > 4A$, the two curves nearly overlap, and the increment of the electromagnetic force with increasing I gradually decreases. The phenomena can be explained with

the B-H curve of the iron core and armature.” [Zhao et al., 2017a]

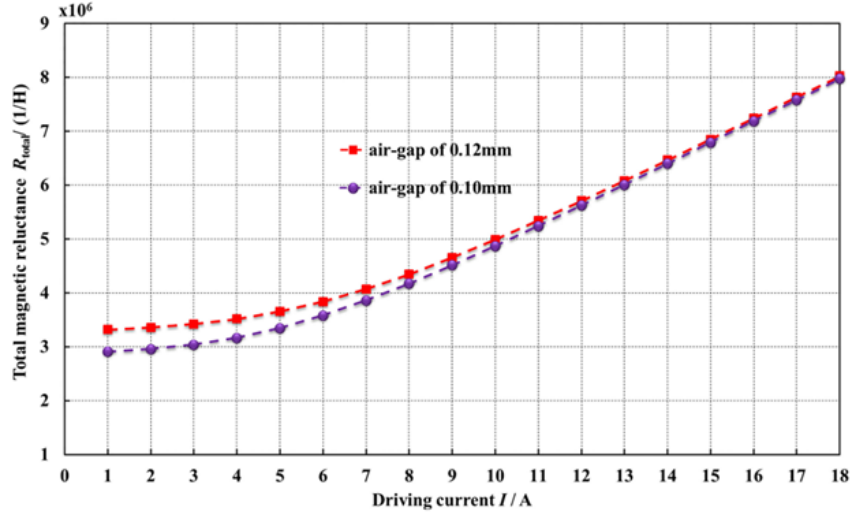


Figure 2.5: Influence of driving current on total magnetic reluctance at different working air gaps [Zhao et al., 2017a]

As seen in fig. 2.5, change $\partial R / \partial I$ starts to dominate the total magnetic reluctance. The researchers conclude that “increasing I will cause premature saturation in the HSV, and the magnetic reluctance of the soft magnetic material will become a decisive factor in restricting the variation of the total magnetic reluctance, which causes the changes of the total magnetic reluctance at different working air gaps to be the same with increasing I . Therefore, it can be surmised that when $I > 4A$, the electromagnetic forces with different working air gaps will increase at the same rate with increasing I .” [Zhao et al., 2017a]

The fig 2.6 show us the B-H curve and it shows how magnetic saturation occurs. To increase the materials magnetic flux density one must exponentially increase the magnetic field intensity which results in high power consumption or is limited by solenoids current carrying capacity. “ I and the working air gap both have significant effects on the variation of the total magnetic reluctance. Too large current or small working air gap will lead to the saturation of magnetic circuit.” [Zhao et al., 2017a] For an efficient solenoid system the air gap should have the highest magnetic reluctance contribution to the total magnetic reluctance.

“Fig 2.7 shows that at different values of I , the electromagnetic force decreases

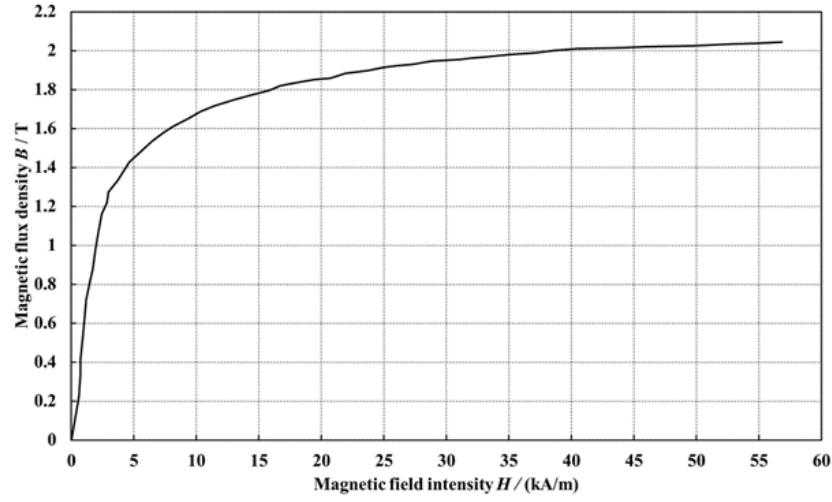


Figure 2.6: The B-H curve of the iron core and armature. [Zhao et al., 2017a]

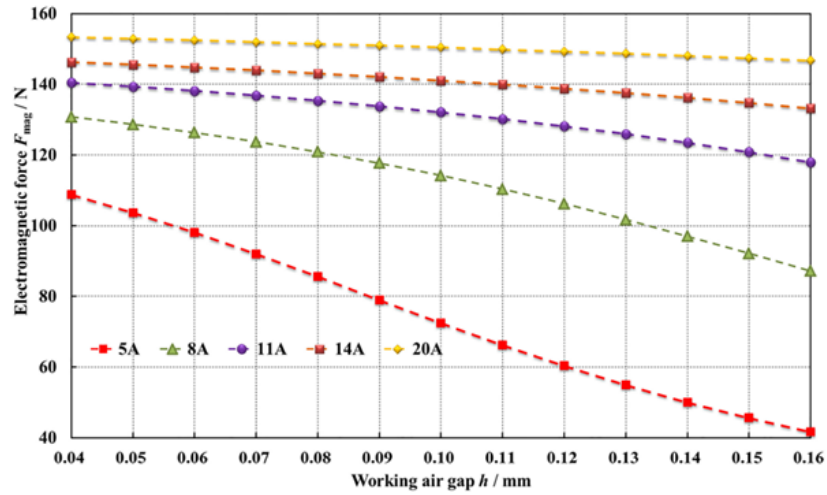


Figure 2.7: Influence of h on the electromagnetic force at different driving currents [Zhao et al., 2017a] (x axis is in 10mm)

with an increasing of the working air gap, and the rate of decrease is affected by the value of I . The larger I becomes, the smaller the rate is.” [Zhao et al., 2017a] This occurs because the magnetic reluctance caused by saturation dominates the magnetic reluctance due to the air gap.

The fig. 2.8 “shows that at different values of I , the total magnetic reluctance increases with an increase of the working air gap. When the total magnetic flux is constant, the electromagnetic force decreases with increasing total magnetic reluc-

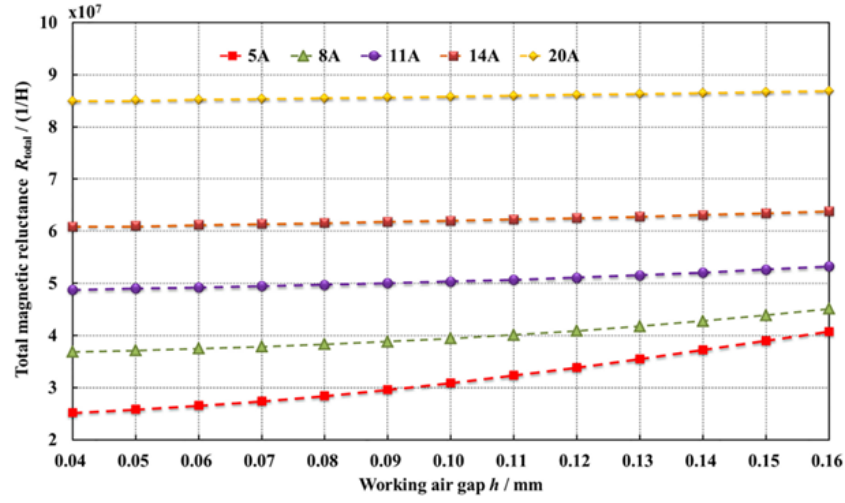


Figure 2.8: Influence of h on the total magnetic reluctance at different driving currents [Zhao et al., 2017a] (x axis is in 10mm)

tance. If I is small, the capability of electromagnetic energy conversion in the HSV will be significantly influenced by the working air gap. But if I is large enough to lead to the magnetic saturation, the working air-gap has only a minor influence.” [Zhao et al., 2017a]

2.1.2 $N \cdot I$ (Ampere Turns)

As seen in eq. 2.1, magneto motive force is linearly proportional to $N \cdot I$. There is however a limit to this relationship. In fig. 2.9 Yang et al. shows that magneto motive force is saturated. It should be noted that for different air gaps (range of linear motion) the saturation level varies. Different air gap distances result in exponential increase in air gap magnetic reluctance. Thus it requires more ampere turns to increase the magnetic reluctance of the magnetic circuit to match and exceed the air gap.

2.2 Armature Surface Area

Armature surface area perpendicular to the magnetic flux acting on it is crucial in determining magneto motive force as seen in eq. 2.1. Yang et al. improved the efficiency of a micro digital valve by changing the design in such a way that they

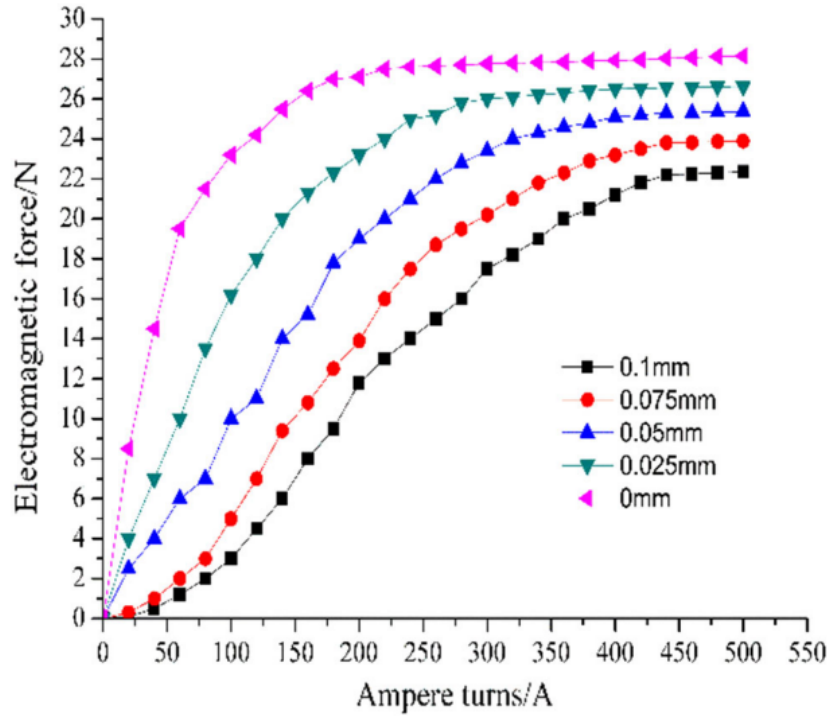


Figure 2.9: Electromagnetic force of different Ampere-turns [Yang et al., 2019]

increased the armature surface area which led to an increase in magnetic flux thus increasing the magneto motive force for the same $N \cdot I$ [Yang et al., 2019].

“Under the same displacement of the iron core, the testing results of electromagnetic force of the novel micro high-speed digital valve were about 1.33 times as that of the traditional valve. ... ratio of the testing results was in good agreement with the area ratio of the two valves.” [Yang et al., 2019]

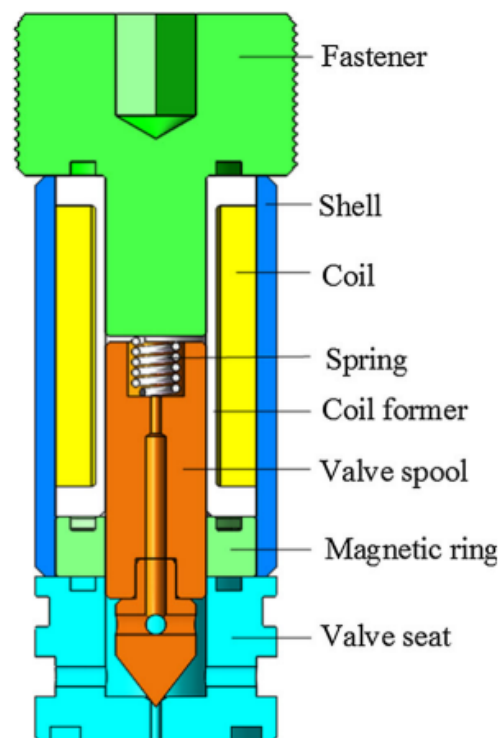


Figure 2.10: Traditional micro high-speed digital valve [Yang et al., 2019]

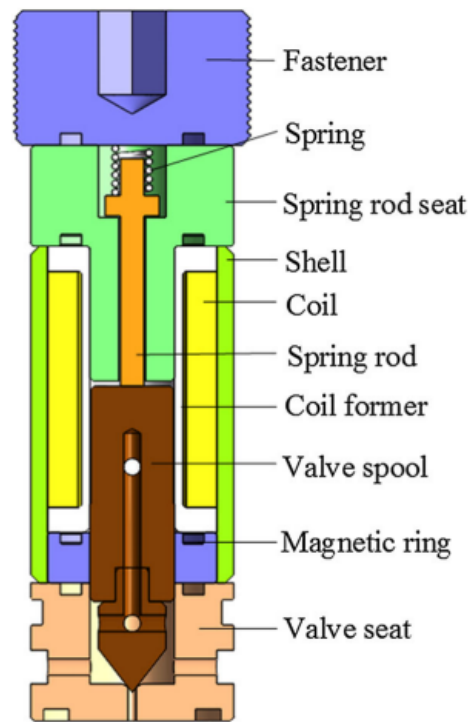


Figure 2.11: Novel micro high-speed digital valve [Yang et al., 2019]

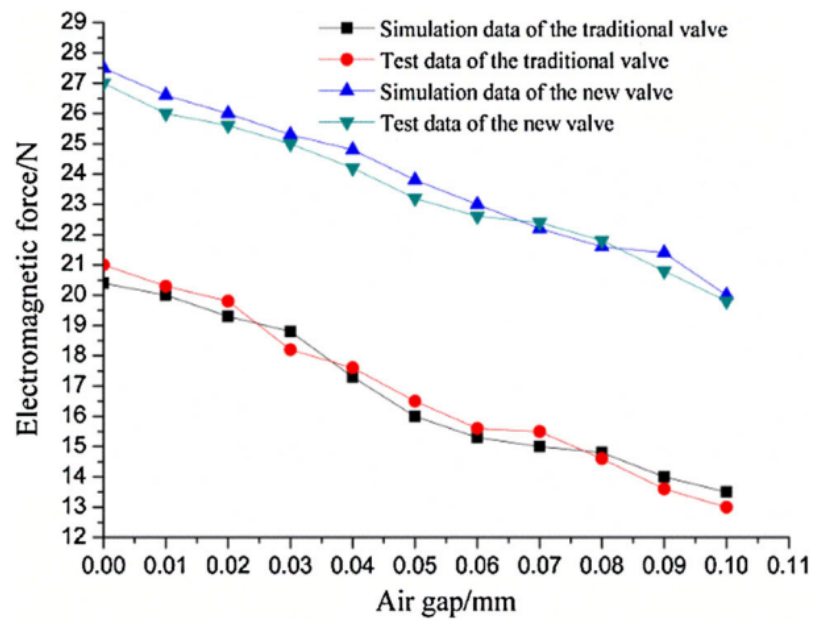


Figure 2.12: Electromagnetic force for different arrangement [Yang et al., 2019]

Chapter 3

MAGNETIC MODEL OF A SOLENOID VALVE

In this chapter we will be modelling the magnetic circuit of the HSV by Yang et al. from the previous chapter.

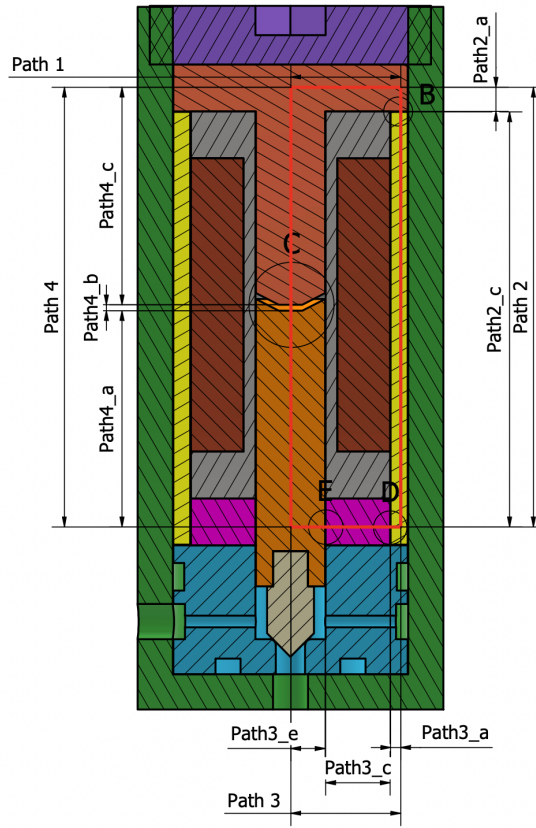


Figure 3.1: Magnetic path shown on assembly

As seen in Fig. 3.1, magnetic circuit is divided into 4 linear sections following the method of Zhao et al. *Path1* is uninterrupted and flows through the part labeled as magnetic top.

$$R_{\text{path1}} = \frac{4 r_{\text{Cout}}}{\mu \mu_0 t_{\text{mta}} \pi (c_a + c_r + 2 r_{\text{Cout}} + t_{\text{shell}})} \quad (3.1)$$

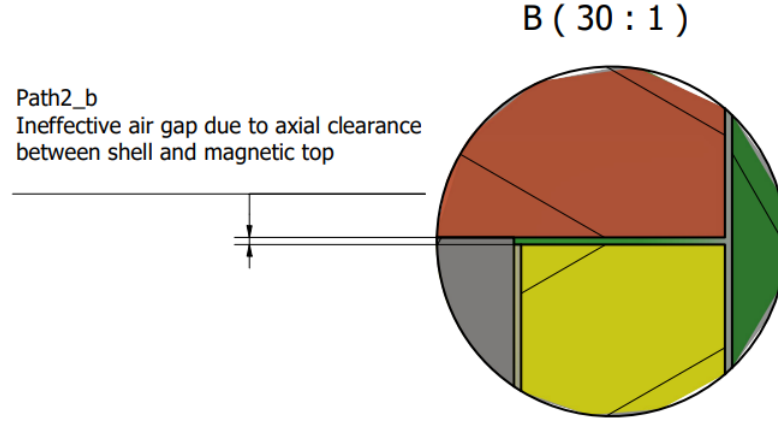


Figure 3.2: Detail view on vertical air gap between magnetic top and shell.

Path 2 is divided into 3 sections. $Path2_a$ is the outer vertical path through the magnetic top. $Path2_b$ is the vertical path through the ineffective air gap due to axial clearance between shell and magnetic top shown in Fig. 3.2. $Path2_c$ is the path through shell.

$$R_{\text{path2}} = \frac{c_a}{\mu_0 \pi ((c_r + r_{\text{Cout}} + t_{\text{shell}})^2 - (c_r + r_{\text{Cout}})^2)} + \frac{h_C - c_a + 2 t_{\text{cfa}} + \frac{t_{\text{mba}}}{2} + t_{\text{mta}}}{\mu \mu_0 \pi ((c_r + r_{\text{Cout}} + t_{\text{shell}})^2 - (c_r + r_{\text{Cout}})^2)} \quad (3.2)$$

Path 3 is divided into 5 sections. $Path3_a$ is the horizontal path through shell. $Path3_b$ is the path through ineffective air gap due to radial clearance between shell and magnetic bottom shown in Fig. 3.3. $Path3_c$ is the horizontal path through magnetic bottom. $Path3_d$ is the path through ineffective air gap due to radial clearance between shell and magnetic bottom shown in Fig. 3.4. $Path3_e$ is the horizontal path through the armature.

$$\begin{aligned}
R_{\text{path3}} = & \frac{2}{\mu \mu_0 t_{\text{mba}} \pi} + \\
& \frac{c_r}{\mu_0 t_{\text{mba}} \pi \left(\frac{c_r}{2} + r_A \right)} + \\
& \frac{c_r}{\mu_0 t_{\text{mba}} \pi \left(\frac{c_r}{2} + r_{\text{Cout}} \right)} + \\
& \frac{t_{\text{shell}}}{2 \mu \mu_0 t_{\text{mba}} \pi \left(c_r + r_{\text{Cout}} + \frac{t_{\text{shell}}}{2} \right)} - \\
& \frac{2 (c_r + r_A - r_{\text{Cout}})}{\mu \mu_0 t_{\text{mba}} \pi (c_r + r_A + r_{\text{Cout}})}
\end{aligned} \tag{3.3}$$

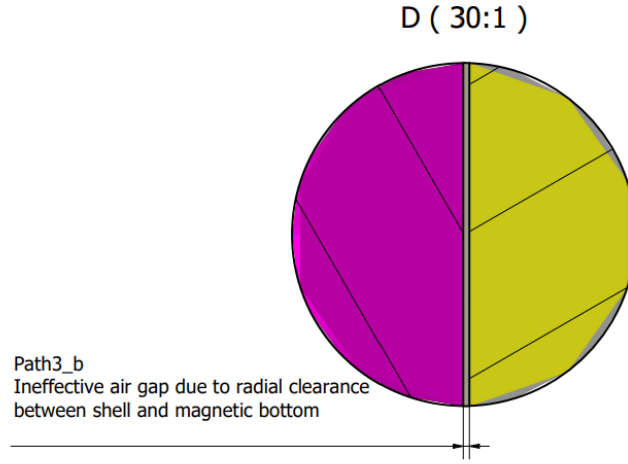


Figure 3.3: Detail view on horizontal air gap between shell and magnetic bottom.

Path 4 is divided into 3 sections. $Path4_a$ is the vertical path through the armature. $Path4_b$ is the path through the effective air gap shown in Fig. 3.5 where the use full magneto motive force is generated. $Path4_c$ is the vertical path through magnetic top.

The effective air gap $Path4_b$ is further divided into 2 sections. $Path4_{b1}$ is where opposing faces are horizontal and the magnetic flux through is vertical, therefore the magnetic reluctance of $Path4_{b1}$ is:

$$R_{Path4_{b1}} = \frac{h_{\text{air}}}{\mu_0 r_{\text{cham}}^2 \pi} \tag{3.4}$$

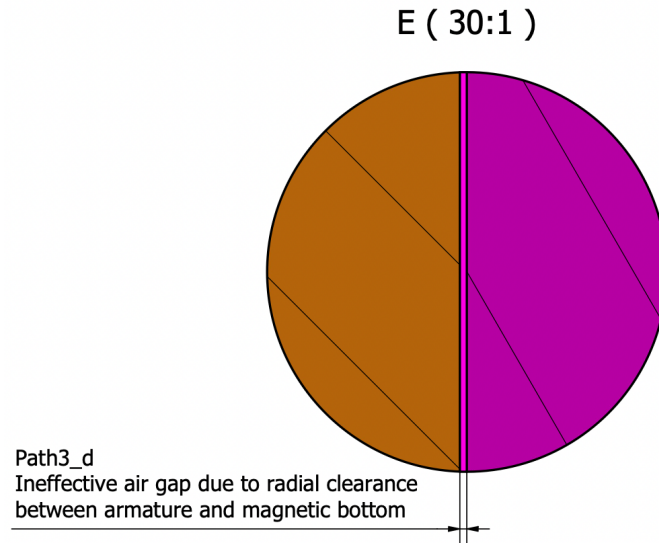


Figure 3.4: Detail view on horizontal air gap between magnetic bottom and armature.

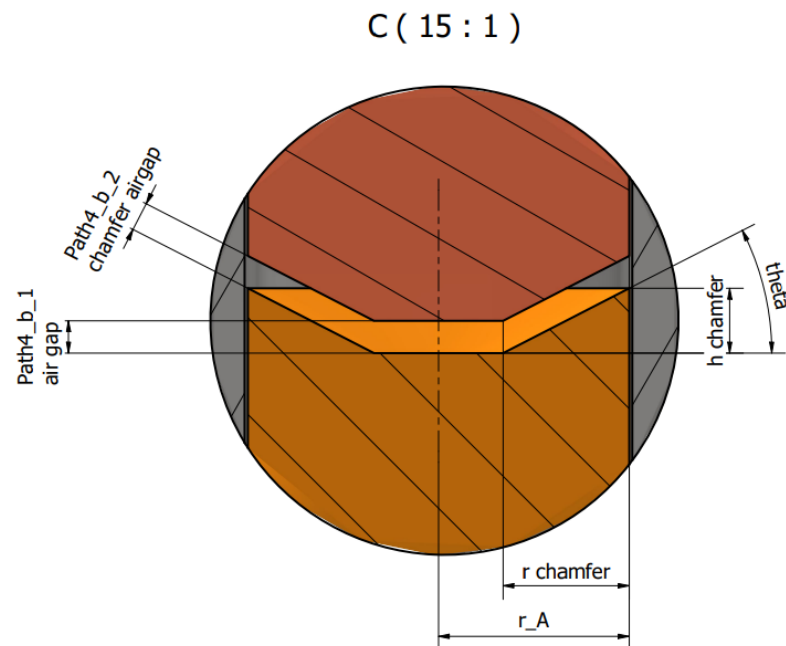


Figure 3.5: Detail view on vertical effective air gap between magnetic top and armature.

Computing $Path4_{b1}$ is trickier. First we compute

$$\theta = \text{atan}\left(\frac{h_{\text{cham}}}{r_{\text{cham}}}\right) \quad (3.5)$$

$$h_{\text{chamferAirgap}} = h_{\text{air}} \cos(\theta) \quad (3.6)$$

and then we assumed that

$$A_{\text{chamfer}} = \pi (r_A^2 - (r_A - r_{\text{cham}})^2) \quad (3.7)$$

When we apply the eq. 2.3 we compute $Path4_{b2}$ as the following:

$$R_{Path4_{b2}} = \frac{h_{\text{air}}}{\mu_0 \pi \left(\frac{h_{\text{cham}}^2}{r_{\text{cham}}^2} + 1 \right) (r_A^2 - (r_A - r_{\text{cham}})^2)} \quad (3.8)$$

Total effective reluctance $Path4_b$ is computed with the following assumption for parallel magnetic flux in eq 3.9

$$\frac{1}{R_{\text{combined}}} = \frac{1}{R_1} + \frac{1}{R_2} + \dots + \frac{1}{R_n} \quad (3.9)$$

$$\frac{1}{R_{\text{combined}}} = \frac{1}{R_{Path4_{b1}}} + \frac{1}{R_{Path4_{b2}}} \quad (3.10)$$

$Path4_b$ is computed and simplified in eq. 3.11.

$$\begin{aligned} R_{\text{combined}} &= \frac{1}{\frac{1}{R_{Path4_{b1}}} + \frac{1}{R_{Path4_{b2}}}} \\ &= \frac{1}{\frac{\pi \mu_0 (r_A - r_{\text{cham}})^2}{h_{\text{air}}} - \frac{\pi \mu_0 \left(\frac{h_{\text{cham}}^2}{r_{\text{cham}}^2} + 1 \right) ((r_A - r_{\text{cham}})^2 - r_A^2)}{h_{\text{air}}}} \\ &= \frac{h_{\text{air}} r_{\text{cham}}}{\mu_0 \pi (2 h_{\text{cham}}^2 r_A - r_{\text{cham}} h_{\text{cham}}^2 + r_{\text{cham}} r_A^2)} \end{aligned} \quad (3.11)$$

$$\begin{aligned} R_{Path4} &= \frac{c_a + \frac{h_C}{2} - h_{\text{air}} + t_{\text{cfa}} + \frac{t_{\text{mba}}}{2}}{\mu \mu_0 r_A^2 \pi} + \\ &\quad \frac{h_{\text{air}} r_{\text{cham}}}{\mu_0 \pi (2 h_{\text{cham}}^2 r_A - r_{\text{cham}} h_{\text{cham}}^2 + r_{\text{cham}} r_A^2)} + \\ &\quad \frac{c_a + \frac{h_C}{2} + t_{\text{cfa}} + \frac{t_{\text{mta}}}{2}}{\mu \mu_0 r_A^2 \pi} \end{aligned} \quad (3.12)$$

$$R_{\text{total}} = R_{Path1} + R_{Path2} + R_{Path3} + R_{Path4} \quad (3.13)$$

After computing the total reluctance we can compute the magnetic flux using the eq. 2.2 and the magneto motive force using the eq. 2.1.

Chapter 4

DYNAMIC MODEL OF A SOLENOID VALVE

4.1 Mechanical Model

The only moving part in this direct acting solenoid part is the armature. The normally closed solenoid valve is turned on and off via applying a voltage on the solenoid leads that creates the magneto motive force and lets the fluid flow through. In fig. 4.1 we present the forces acting on the armature. F_{mm} is the magneto motive force, F_{airgap} is the force generated by the fluid pressure in the air gap on the top surface of the armature, $F_{chamber}$ is the generated by the fluid pressure in the chamber on the bottom surface of the armature and F_{spring} is the force generated by the compression spring. This free body diagrams describes the dynamic behaviour of the valve.

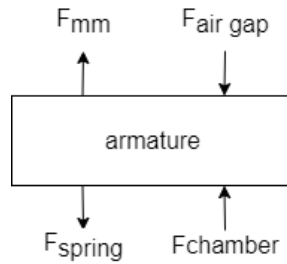


Figure 4.1: Armature Free Body Diagram

In section 2 we showed how to compute F_{mm} for a given design, armature position and applied current.

$$F_{mm} = \frac{1 \cdot \phi^2}{2 \cdot \mu_0 \cdot S_2} \quad (2.1)$$

$$F_{airgap} = \pi r_A^2 P_{airgap} \quad (4.1)$$

$$F_{chamber} = \pi r_A^2 P_{chamber} - \pi r_{orifice}^2 P_d \quad (4.2)$$

$$F_{spring} = (x + x_0) * k_s \quad (4.3)$$

where x_0 stands for the pre-loading of the spring and k_s is the spring constant

$$F(t) = F_{mm}(t) - F_{airgap}(t) + F_{chamber}(t) - F_{spring}(t) \quad (4.4)$$

$$F(t) = m \ddot{x}(t) \quad (4.5)$$

$$\dot{x}(t) = \dot{x}(t-1) + \ddot{x}(t-1) dt \quad (4.6)$$

$$x(t) = x(t-1) + \dot{x}(t-1) dt + \ddot{x}(t-1) dt^2 \quad (4.7)$$

The mass of the armature can be computed from the material density (430F SS for this model) ρ and the armature geometry.

$$m = r_A^2 \rho \left(\frac{h_C}{2} + t_{cfa} \right) \quad (4.8)$$

4.2 Electrical Model

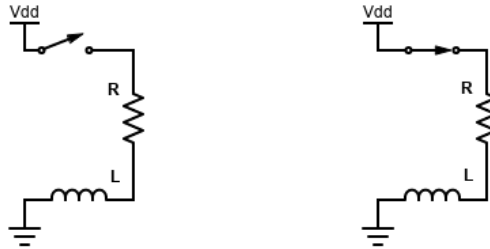


Figure 4.2: Schematic of electrical circuit. (left) Valve powered off. (right) Valve powered on.

In fig. 4.2 the electrical schematic of the valve is presented. A solid state relay (SSR) is used to switch the solenoid on and off and any losses due to wiring and SSR is ignored in the model. We can represent the schematic with the following equations:

$$\begin{aligned} V_{dd} &= V_L + V_R \\ &= L di + R i \end{aligned} \quad (4.9)$$

$$V_{dd} = L(t) \frac{di}{dt}(t) + R i(t) \quad (4.10)$$

Assuming V_{dd} is constant we can compute $\frac{di}{dt}$ with the following derivation:

$$V_L(t) = V_{dd} - R i(t) \quad (4.11)$$

$$\frac{di}{dt}(t) = \frac{V_L(t)}{L(t)} \quad (4.12)$$

We can compute the inductance of the solenoid system using the eq. 4.13. Inductance will play a crucial role in the dynamic analysis of the solenoid valve. Inductance will dictate the reaction time of the solenoid valve.

$$L = \frac{N \phi}{i} = \frac{N^2}{R_{total}} \quad (4.13)$$

We can compute the resistance R from coil geometry (R_{Cin} coil inner radius, R_{Cout} coil outer radius), winding number N , wire diameter d_w and electrical resistivity of the conductor ρ as follows:

$$R = \pi (r_{Cout} + r_{Cin}) N \rho \quad (4.14)$$

Finally we can compute $i(t)$ with the following equation:

$$i(t) = i(t-1) + \frac{di}{dt}(t-1) dt \quad (4.15)$$

Notice in fig. 4.2 that the circuit is a LR circuit. Valve reaction time is an important performance metric for solenoid valves. Generally it is assumed that 3τ is the time that the valve is fully opened. Valve closing time on the other hand depends on the spring constant k_s and pressure balance between chamber and air gap. This will be discussed in the next section.

$$\tau = \frac{L}{R} \quad (4.16)$$

Notice in eq. 4.13 inductance varies with magnetic flux, thus varies by R_{total} . This results in different time constants for different armature positions. For this dynamic model, a positive voltage will be applied for $4\tau_{opening}$ seconds. After this duration the voltage will be removed and the simulation will be run for another $4\tau_{closing}$ seconds.

$$\tau_{opening} = \frac{L(h_{air})}{R} \quad (4.17)$$

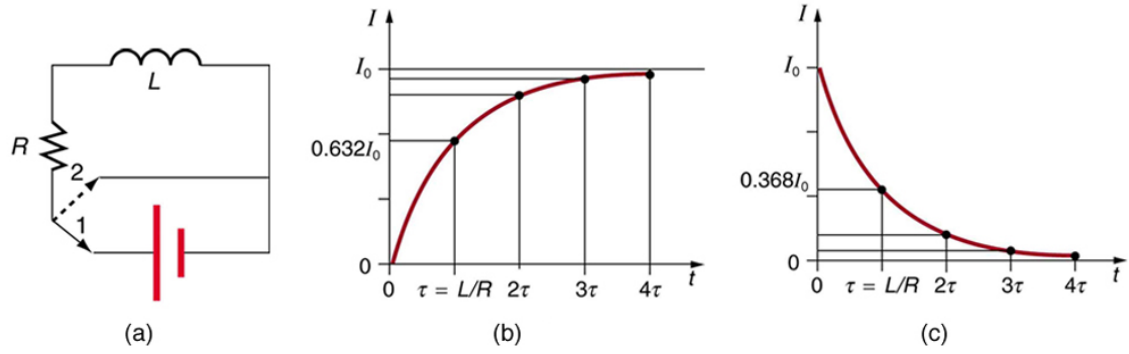


Figure 4.3: (a) An RL circuit with a switch to turn current on and off. When in position 1, the battery, resistor, and inductor are in series and a current is established. In position 2, the battery is removed and the current eventually stops because of energy loss in the resistor. (b) A graph of current growth versus time when the switch is moved to position 1. (c) A graph of current decay when the switch is moved to position 2.[OpenStax, 2022]

$$\tau_{closing} = \frac{L(c_a)}{R} \quad (4.18)$$

In eq. 4.17 the inductance is computed with the maximum air gap and in eq. 4.18 the inductance is computed with minimum air gap that is equal to the axial clearance c_a .

4.3 Simulation Meta Data

Simulation time step is set to $1\mu s$, $10^{-6}s$, in order to account for the dynamic nature of the simulation. As it is presented in the next section, mass flows and the change in pressures and temperatures are integrated through the simulation. A small time step is required to keep the simulation stable. For step sizes above $1\mu s$ the simulation diverges due to small control volumes and high flow rates.

4.4 Flow Model

The valve design has 2 control volumes. These control volumes are V_{airgap} and $V_{chamber}$. The states of these volumes are defined by their volume V , temperature T , density ρ and mass M . The interaction between these control volumes are defined by the armature radial clearance flow path. This flow path is defined by a flow cross

section area A_{rc} and a discharge coefficient $C_{d,rc}$.

The valve is placed between two reservoirs, upstream and downstream. For this model the upstream and downstream reservoirs are assumed to be infinite and have constant temperature and density. The interaction between the chamber and the reservoirs are defined by inlet and outlet orifices. These orifices are defined by r_{inlet} , $C_{d,inlet}$, r_{outlet} and $C_{d,outlet}$. Outlet orifice is open gradually due to the mechanics of the armature. This is taken in to account by multiplying the effective area with the armature travel percentage.

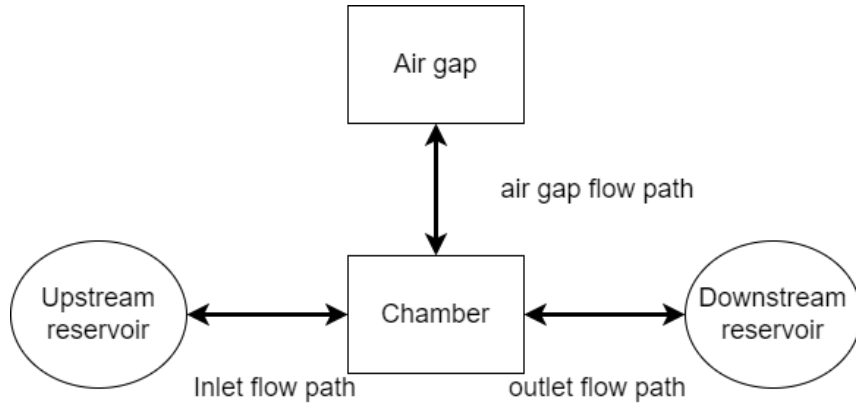


Figure 4.4: Abstraction of valve volumes, and flow paths.

The following subsections will present the simulation algorithm in the order of execution for each loop.

4.4.1 Armature Motion

The armature motion is computed with the forces computed in the previous loop with order: eqs. 4.5, 4.6, 4.7. After computing this loops position, velocity and acceleration; if they exceed the range of motion position is capped and velocity and acceleration is set to zero.

4.4.2 Electrical and Magnetic Circuit Simulation

The electrical current for this loop is computed with eq. 4.15. The applied voltage is calculate based on the time in the simulation mentioned in eqs 4.17 and 4.18. R_{total}

is computed with the current armature position and used to calculate current flux with eq. 2.2. F_{mm} is computed with eq. 2.1. Inductance voltage V_L and change in electrical current for next step $\frac{di}{dt}$ is computed with eqs. 4.11 and 4.12.

4.4.3 Control Volume Changes

Volume of the air gap and the chamber changes due to armature translation. This changes the temperature and the pressure in these control volumes. These processes are assumed to be adiabatic compression/expansion because the volume changes happen under in the order of us .

$$P(i) = P(i-1) \left(\frac{V(i-1)}{V(i)} \right)^\gamma \quad (4.19)$$

$$T(i) = T(i-1) \left(\frac{V(i-1)}{V(i)} \right)^{(\gamma-1)} \quad (4.20)$$

4.4.4 Gas Flows

It is assumed that the flow velocities at the inlet, outlet and the radial clearance around the armature are normal to the flow restriction surfaces. It is also assumed that all intensive properties (specific internal energy, specific volume, specific enthalpy, temperature, pressure and specific entropy) are uniform over the flow restriction surfaces, thus the flow is assumed to be 1D.

The order of gas flow computation is from downstream to upstream. First the mass flow from chamber to downstream reservoir $\dot{m}_{c,d}$ and its effects on the $M_{chamber}$, $P_{chamber}$ and $T_{chamber}$ are computed. Then the mass flow between chamber and air gap $\dot{m}_{c,a}$ and its effects on $M_{chamber}$, $P_{chamber}$, $T_{chamber}$, M_{airgap} , P_{airgap} and T_{airgap} are computed. Finally the mass flow from upstream reservoir to chamber $\dot{m}_{u,c}$ and its effects on the $M_{chamber}$, $P_{chamber}$ and $T_{chamber}$ are computed.

Computing Flow Velocity

$$M = \sqrt{\left(\frac{P_{high}}{P_{low}} \right)^{\left(\frac{\gamma-1}{\gamma} \right)} \frac{2}{\gamma-1}} \quad (4.21)$$

Flow velocity between two pressure reservoirs is computed by the eq. 4.21 derived from the adiabatic flow equation [NASA, 2021]. If the resulting Mach number M is greater than 1, it is capped to 1 because the flow through orifices is choked.

Computing Mass Flow Rate

After computing flow velocity M one can compute the mass flow rate \dot{m} using the eq. 4.22 [NASA, 2021], where A is the orifice surface area, P_t is the total/upstream pressure, T_t is the total/upstream temperature, R is the gas constant, γ is the ratio of specific heats for the gas and C_d is the discharge coefficient for the given flow restriction area.

$$\dot{m} = C_d \frac{A P_t}{\sqrt{T_t}} \sqrt{\frac{\gamma}{R}} M \left(1 + \frac{\gamma - 1}{2} M^2 \right)^{-\frac{\gamma+1}{2(\gamma-1)}} \quad (4.22)$$

Computing Gas Charge/Discharge

After computing the mass flow rate \dot{m} between two control volumes/reservoirs, the new mass M , pressure P and temperature T should be computed for the control volumes.

$$\Delta m = \dot{m} dt = M(i) - M(i - 1) \quad (4.23)$$

$$M(i) = M(i - 1) + \Delta m \quad (4.24)$$

To compute the next state of the control volumes it is assumed that the process is adiabatic. Thus we can write the following energy and mass conservation.

$$\Delta m = M(i) - M(i - 1) \quad (4.25)$$

$$\Delta e = U(i) - U(i - 1) = H \quad (4.26)$$

$$\Delta e = M(i) u(i) - M(i - 1) u(i - 1) = \Delta m h \quad (4.27)$$

$$0 = \Delta m h - M(i) u(i) + M(i - 1) u(i - 1) \quad (4.28)$$

$$0 = \Delta m P v - M(i) C_v T(i) + M(i - 1) C_v T(i - 1)$$

Eq. 4.28 leverages the fact that work done by entering/exiting gas can be computed using its enthalpy to simplify the expression.

$$T(i) = \frac{U(i)}{M(i) C_v} \quad (4.29)$$

$$P(i) = \frac{RT(i)}{v} \quad (4.30)$$

Control volume states are computed with the equations above with the ideal gas assumptions.

Computing Forces on Armature

Last step of the simulation loop is to compute the forces acting on the armature. These forces are computed with the eqs. 2.1, 4.1, 4.2, 4.3 and 4.4. After computing the net force one can compute the dynamic behavior of the armature using eqs. 4.5, 4.6 and 4.7.

Chapter 5

SIMULATION

Using the model described in the previous chapter we ran the simulation with a time step of 1μ seconds.

Simulation is set with the following parameters:

$$c_r = 0.05mm$$

$$c_a = 0.05mm$$

$$h_C = 25mm$$

$$r_{Cout} = 12mm$$

$$D_w = 0.27mm$$

$$t_{cfr} = 1.5mm$$

$$t_{cfa} = 3mm$$

$$t_{mba} = 1mm$$

$$t_{mta} = 1mm$$

$$r_A = 3.95mm$$

$$r_{cham} = 2mm$$

$$h_{cham} = 2mm$$

$$t_{shell} = 2mm$$

$$PR = 1$$

$$CSF = 0.9$$

$$h_{air} = 0.5mm$$

$$\mu_r = 550$$

$$\mu_0 = 1.25663706212 \cdot 10^{-6} H/m$$

$$CWCC = 10 \cdot 10^6 A/m^2$$

$$erc = 1.68 \cdot 10^{-8} \Omega m$$

$$t_{powered\ on} = 4 \tau_{open}$$

$$t_{powered\ off} = 4 \tau_{close}$$

$$P_u = 50\text{bar}$$

$$P_d = 1\text{bar}$$

$$T_u = T_d = 273\text{K}$$

$$K_{spring} = 25\text{N/mm}$$

$$x_{preload} = 0.5\text{mm}$$

The parameters given above define other properties of the solenoid valve. Total number of winding turns N is set to 2229. Total length of the conductor is set to 122.5m . Resistance of the conductor is set to 36Ω . Maximum current allowed on the circuit is set to 0.5A . The ampere-turns is set to 1149A . The voltage applied to drive the circuit is set to 18.5V . Maximum magnetic field strength that will be reached at peak current is set to 46kA/m . The solenoid time constants are set to $\tau_{open} = 10.9\text{ms}$ and $\tau_{close} = 15.5\text{ms}$.

Another important property of the valve is the outlet orifice area. Outlet orifice area has two effects on the valve. First, it limits the maximum flow rate. Second, when the valve is closed the area over the outlet orifice is sealed and there is a pressure differential that results in a net force. As the orifice area increases so does this force, which results in higher F_{mag} requirements. There is a relation between outlet orifice area and the armature range of motion due to flow restriction area.

$$\begin{aligned} \pi 2 r_{outlet} h_{airgap} &= \pi r_{outlet}^2 \\ 2 h_{airgap} &= r_{outlet} \end{aligned} \tag{5.1}$$

The side surface of the cylinder that has the same radius with the outlet orifice and the height of the air gap should be equal to the surface area of the outlet orifice for optimal flow rate and F_{mag} .

The driving force of this simulation is the effects of the magnetic field generated by the coil. In fig. 5.1, one can observe the change in magnetic flux density with the current applied to the circuit. Note that magnetic flux tapers off while current increases further. This is because of the magnetic saturation simulated using the materials B-H curve. The effect of this saturation can be seen in fig. 5.2.

The magnetic field density increases linearly with the magnetic field strength until the solenoid generates enough force and pulls the armature. When the armature

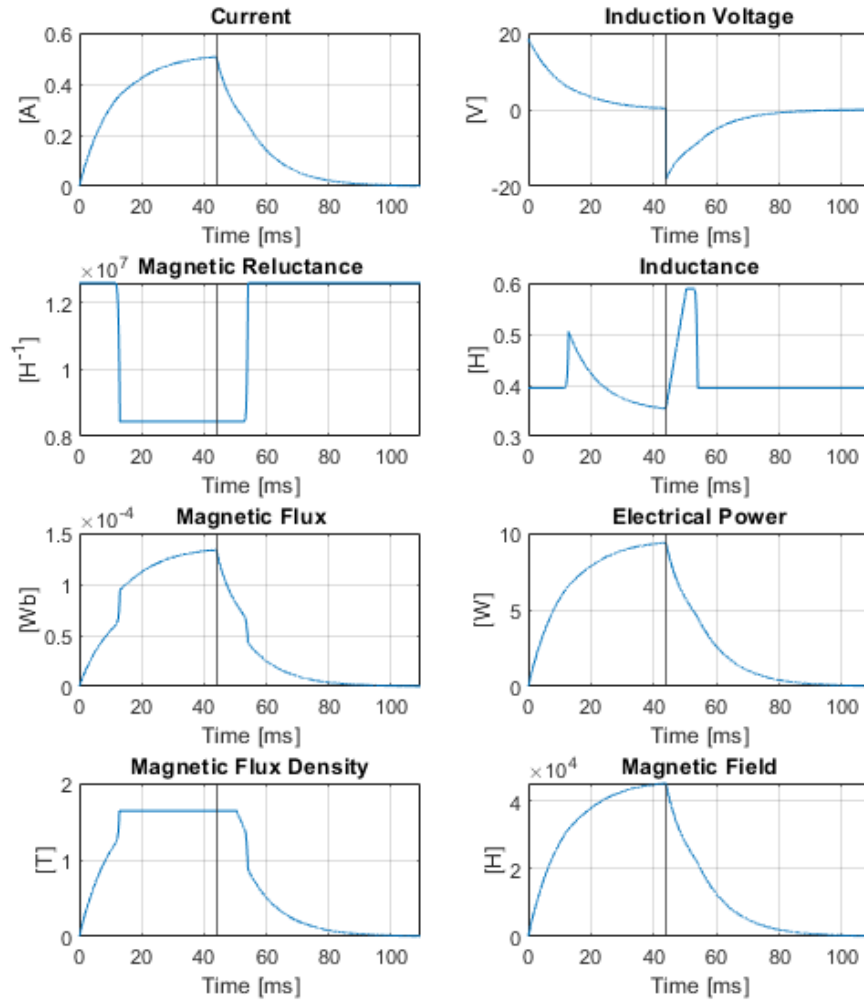


Figure 5.1: Electrical and magnetic circuit development over time.

is fully retracted, the total magnetic reluctance in the circuit diminishes because the effective air gap used to dominate the total reluctance in the magnetic circuit is now filled with 430f SS. After the armature is fully retracted, initially the manufacturing tolerances and clearances start to dominate the total magnetic reluctance but, with increasing magnetic field strength the magnetic permeability of the 430f SS starts to taper off and eventually gets closer to the magnetic permeability of free space μ_0 . This limits the maximum force that can be generated with the given design.

The magneto motive force, F_{mag} , generated tips the force balance on the arma-

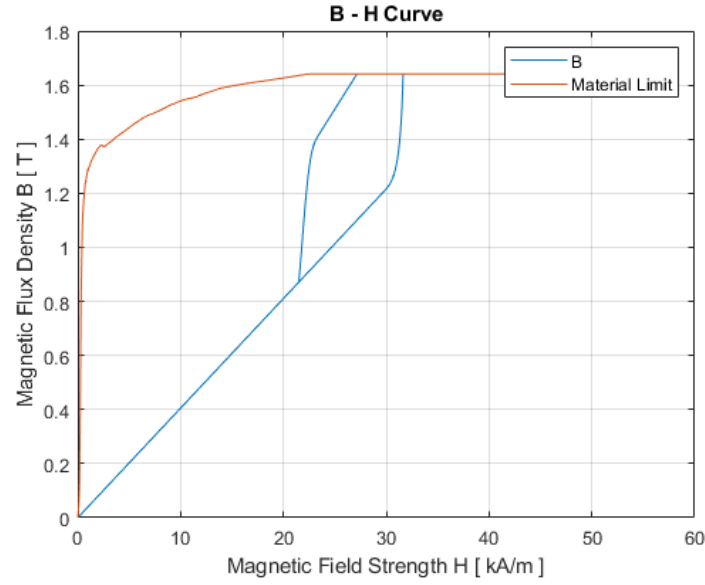


Figure 5.2: Magnetic field strengths and magnetic flux densities reached during simulation.

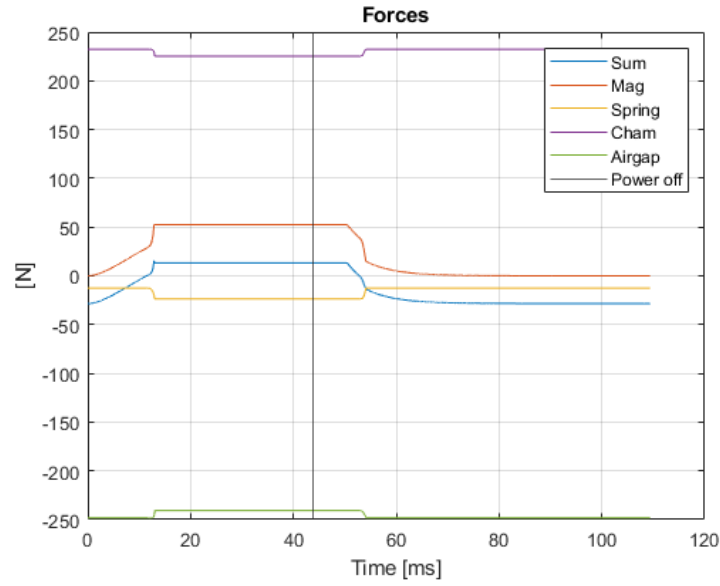


Figure 5.3: All forces acting on the armature.

ture and causes it to retract. In fig. 5.3 all the forces acting on the armature are presented. Notice that magnetic force linearly increases with the applied current until it overcomes the spring and pressure forces. Once the armature starts to retract, the F_{mag} increases exponentially until it is tapered off due to magnetic flux

tapering off. This exponential rise and tapering off can be better seen in fig. 5.4.

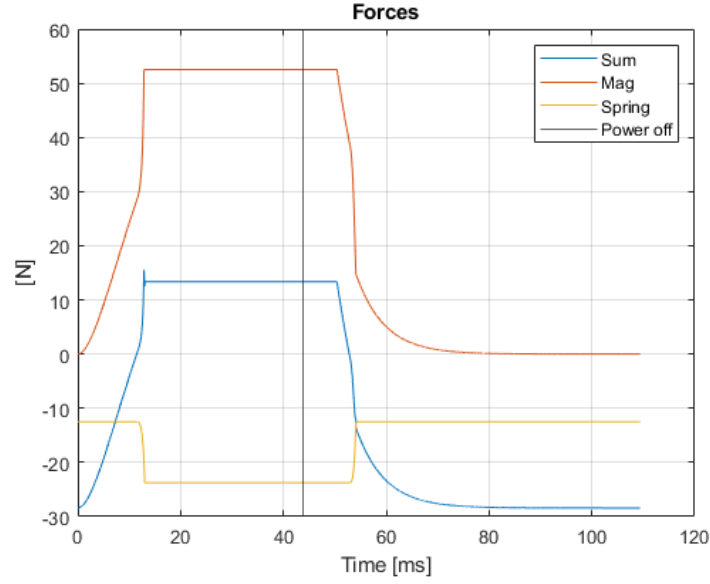


Figure 5.4: Forces acting on the armature excluding pressure forces.

Notice the black vertical line on the plot, it represents the moment the applied voltage is removed. Notice that it takes a considerable amount of time to F_{mag} to diminish. We will further explore this when optimizing the valve to react faster.

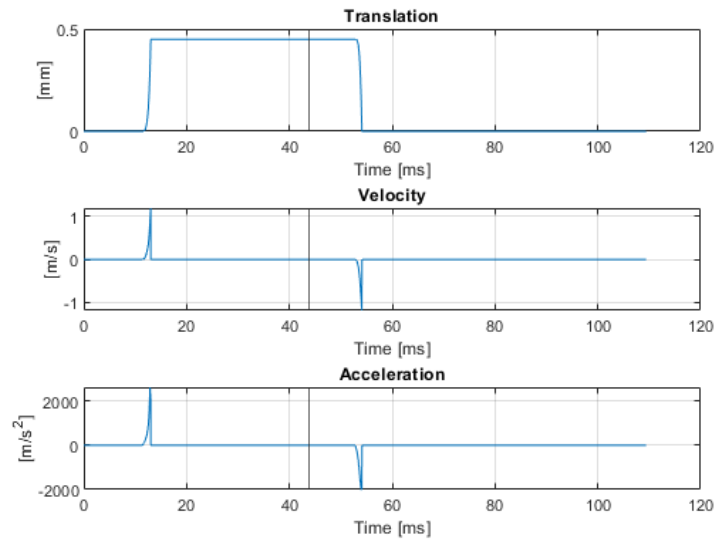


Figure 5.5: Motion on the armature.

In fig. 5.5, the kinematics of the armature are presented. Notice that the actual motion takes a very small time compared to the magnetic field building up or the gas exchange between two chambers.

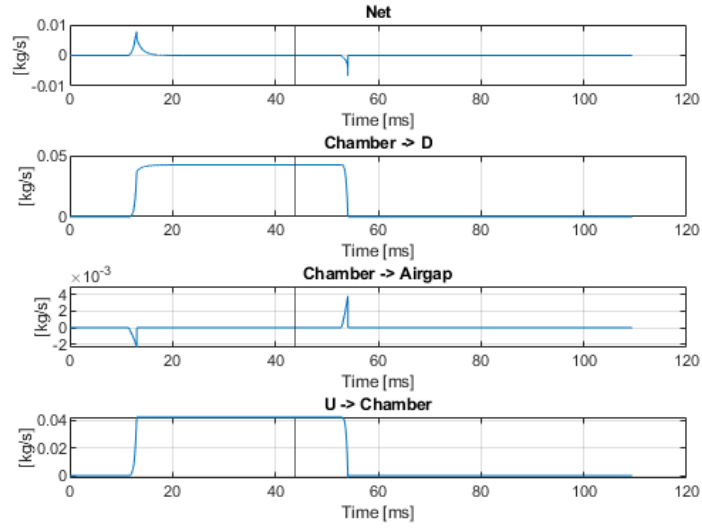


Figure 5.6: Mass flows to and from control volumes.

In fig. 5.6, the effect of armature movement is presented, gas flows from the upstream reservoir to the downstream reservoir through the chamber. Due to armature movement, volumes of the air gap and the chamber changes, this can be seen in fig. 5.9 and 5.10. In this simulation all thermodynamic processes are assumed to be adiabatic, the effect of this assumption can be seen in the rising temperature of the compressed volume. The reverse of same effect is in place in the expanding volume.

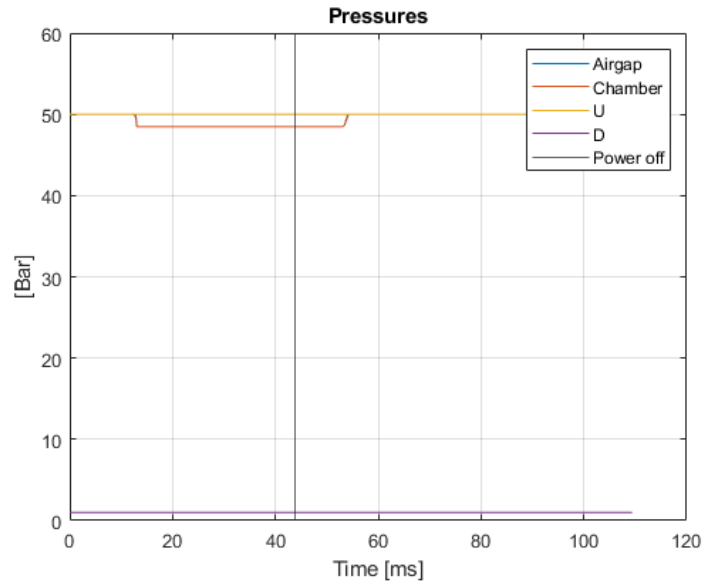


Figure 5.7: Pressures of control volumes and reservoirs.

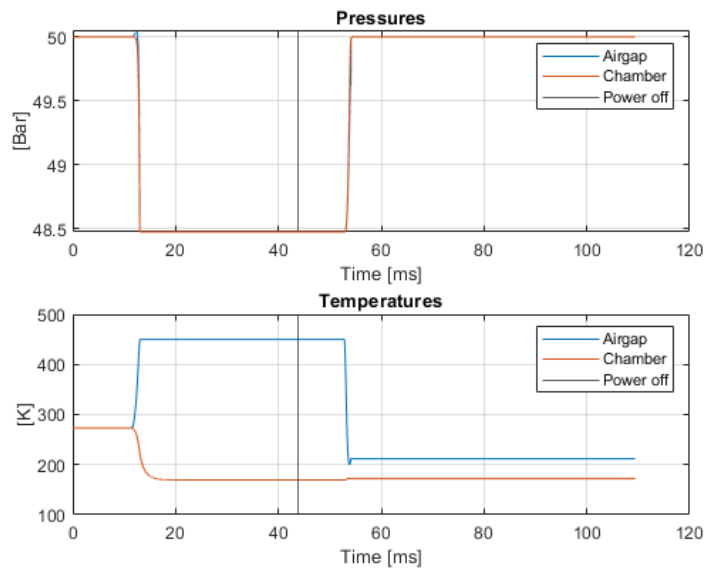


Figure 5.8: Control volume pressure and temperature

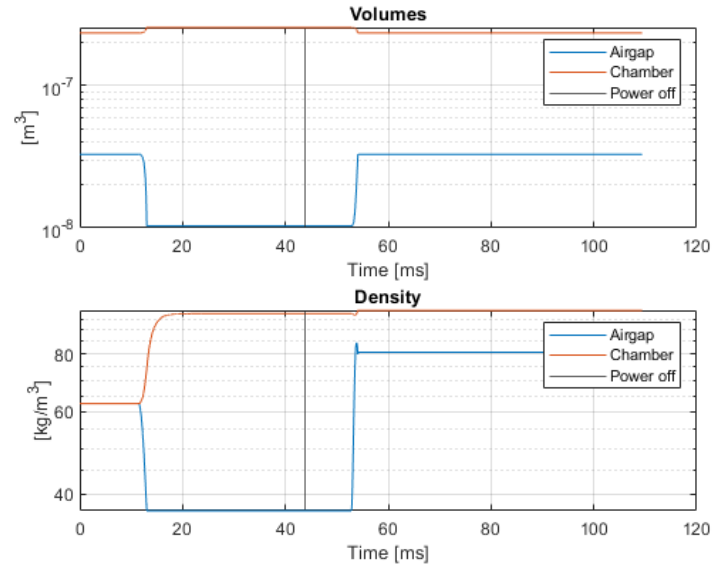


Figure 5.9: Change of the volumes

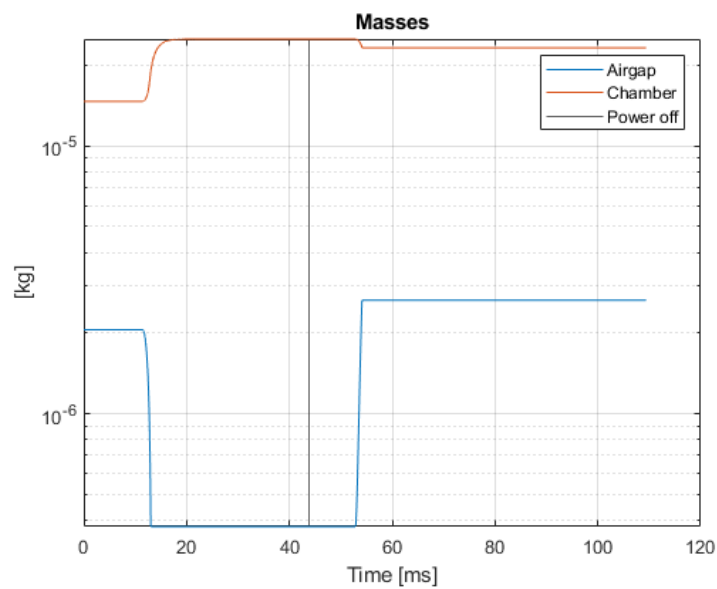


Figure 5.10: Change of the masses

Chapter 6

OPTIMIZATION

In aerospace application there are various uses for solenoid valves. Other than simply be used as valves, in space systems they are used for attitude control thrusters and in rocket applications they can be used as bang-bang pressure regulators. When designing a valve, the weight, the opening time, closing time and power required to operate are important parameters. These parameters should be optimized simultaneously but often there are no single solution which optimized all these parameters at once. Thus, it is important to search the design option space efficiently and account for manufacturing tolerances.

The simulation results presented in the previous chapter is obtained by using the optimized parameters which resulted from multi objective optimization process. Since there are 15 parameters and the permutation of 2 options for each would take 2^{15} iterations, the valve was optimized step by step.

The simulation was also run short to focus on opening and closing events. The driving voltage is applied until the armature is fully retracted. After that the driving voltage was removed and the simulation continued until the armature reached its initial position.

6.1 Cost Functions and Constraints

This multi objective optimization method focuses on 3 independent objectives. These are valve opening time $\tau_{opening}$, valve closing time $\tau_{closing}$ and valve weight. Other performance parameters such as total flow per cycle or total power per cycle are dependent on these objectives.

This multi objective optimization method only searched 10 independent variable spaces out of 15 by diving in to 3 groups which are coil parameters, structural

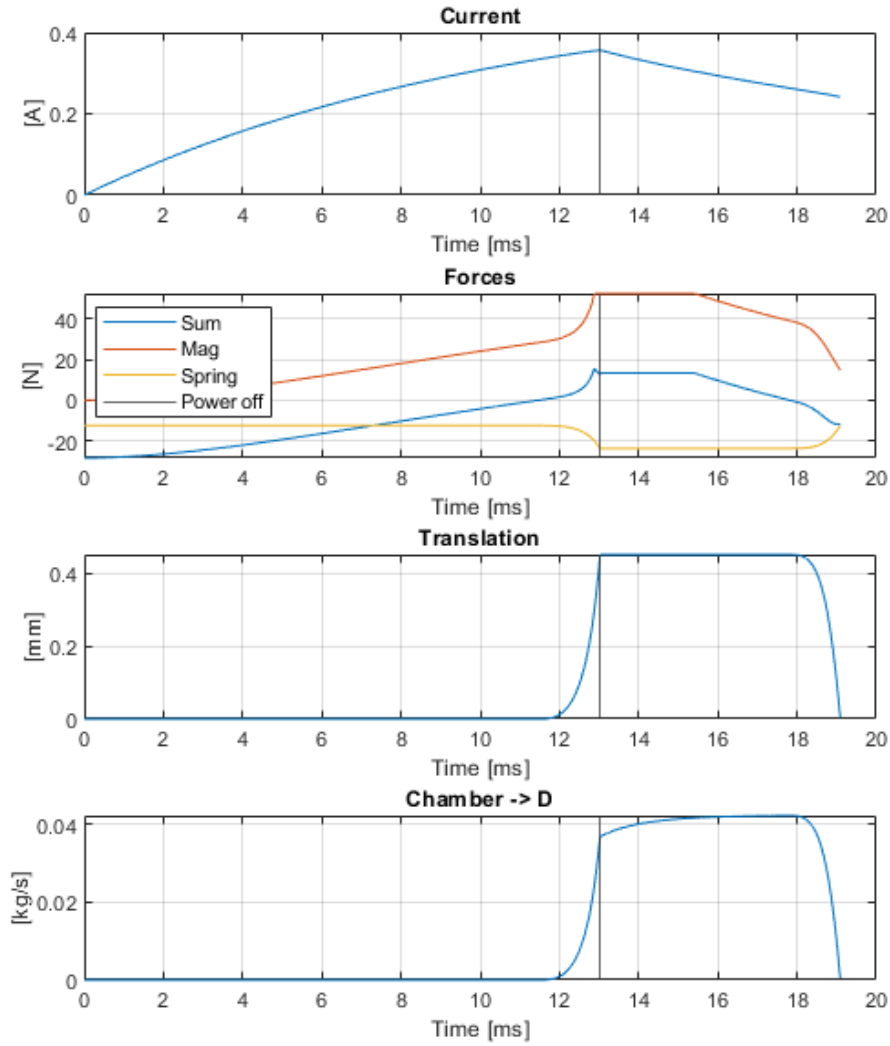


Figure 6.1: Shortened simulation visualization. Simulation and driving voltage start at $t = 0$, and driving voltage is removed at the vertical black line.

elements and manufacturing clearances. Search space constraints and step sizes are presented in each step.

6.2 Optimizing Coil Parameters

There are 3 parameters that dominate coil design and the search space for these were as follows:

$$r_{cout} = 12 : 2 : 20 \text{ mm}$$

$$h_C = 25 : 10 : 75 \text{ mm}$$

$$r_A = 3 : 1 : 5 \text{ mm}$$

After running the simulation there are 3 designs of interest, these are the fastest overall, the one with the minimum mass flow per cycle and the one with the maximum flow rate in oscillating mode. The fig. 6.2 presents us a trade-off between opening and closing time of the valve.

Since the gas flow only occurs when the valve is open and the retraction of the armature takes a fraction of time it is no surprise that the minimum flow per cycle is achieved with the design that has the shortest closing time of them all.

For the maximum flow rate in oscillating mode, the opening time is critical since a reduction in opening time will reduce the time when the valve is in closed position. Therefore the maximum flow rate in oscillating mode is achieved by a design which has one of the fastest opening time and one of the slowest closing time.

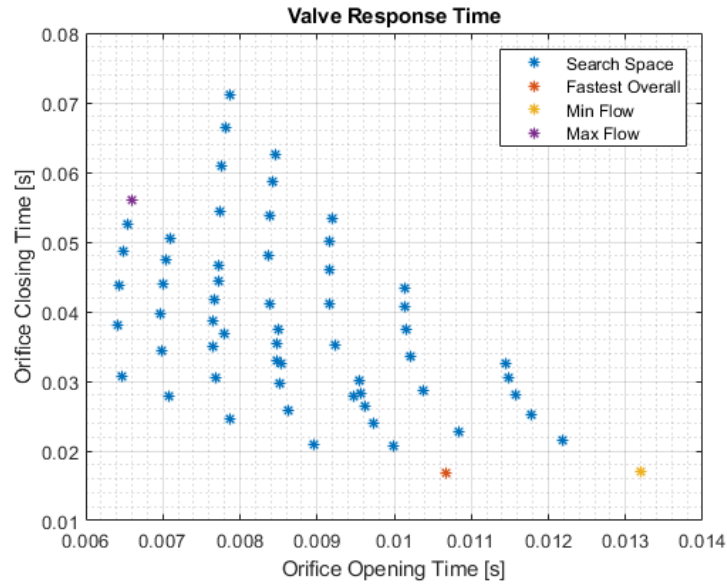


Figure 6.2: Response times of various design options. Trade-offs between opening and closing times.

The fig. 6.3 presents us the trade-off between valve weight and the maximum flow rate in oscillating mode. When picking reaction control thrusters there is trade-off

between thruster frequency and its weight.

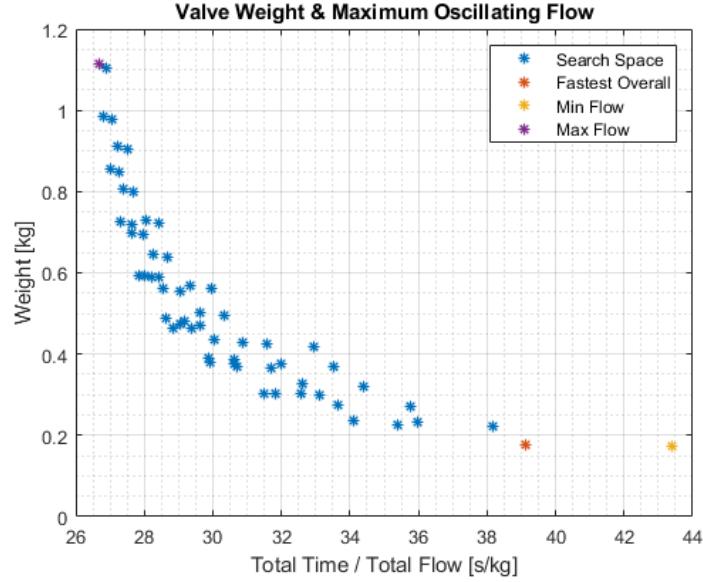


Figure 6.3: x axis represents the time it takes to flow 1 kg of gas during an oscillating valve operation (continuous opening and closing of the valve).

However for a bang-bang regulator the most crucial parameter of a solenoid valve is its closing time/minimum flow. With decreasing minimum flow, the system can be more responsive and precise. Fortunately for us, in our optimization we found that there is not a trade-off between valve weight and its minimum flow capacity as seen in fig. 6.4. The valve with the fastest response was picked and is used in the next optimization steps.

$$r_{cout} = 12 \text{ mm}$$

$$h_C = 25 \text{ mm}$$

$$r_A = 4 \text{ mm}$$

6.3 The Effect of Structural Elements Thickness

After finding the optimal coil parameters, it is time to look into structural parameters and their effects on weight and minimum mass flow per cycle. There are 5 parameters that can be considered as structural elements these were as follows:

$$t_{cfr} = 1 : 0.1 : 1.5 \text{ mm}$$

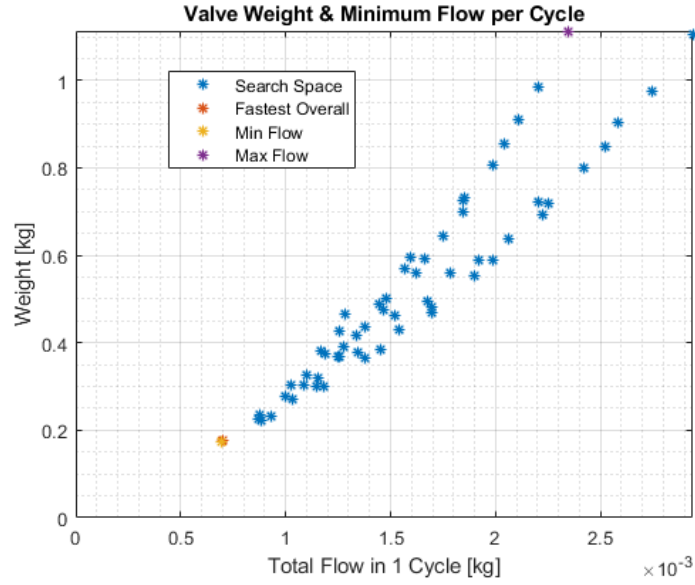


Figure 6.4: Results of simulation: Valve Weight and minimum flow per cycle

$$t_{cfa} = 3 : 1 : 5 \text{ mm}$$

$$t_{mba} = 1 : 1 : 5 \text{ mm}$$

$$t_{mta} = 1 : 1 : 5 \text{ mm}$$

$$t_{shell} = 1 : 1 : 2 \text{ mm}$$

A total of 216 designs were simulated.

Similar to the coil parameter results we see the trade-off between valve opening and closing time. The fastest option is picked for further clearance analysis:

$$t_{cfr} = 1.5 \text{ mm}$$

$$t_{cfa} = 3 \text{ mm}$$

$$t_{mba} = 1 \text{ mm}$$

$$t_{mta} = 1 \text{ mm}$$

$$t_{shell} = 1 \text{ mm}$$

6.4 The Effect of Clearances and Tolerances

It is time to look into clearances, tolearances and their effects on weight and minimum mass flow per cycle. There are 5 parameters that can be considered as struc-

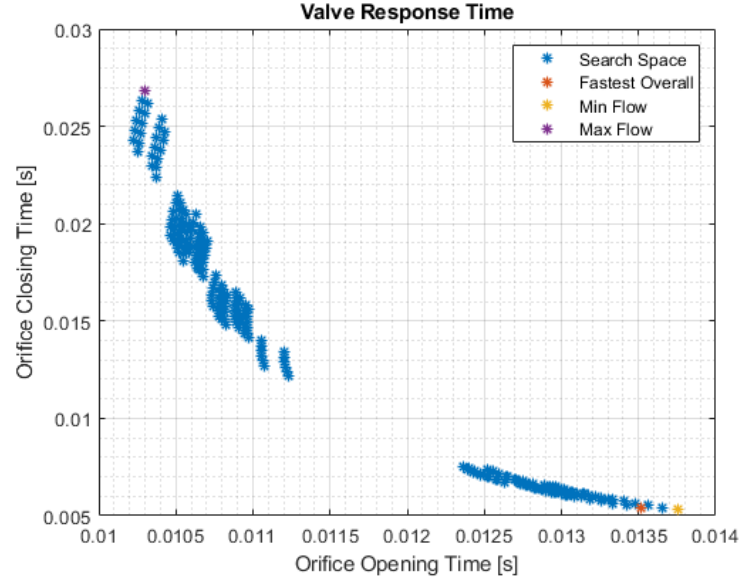


Figure 6.5: Response times of various design options. Trade-offs between opening and closing times.

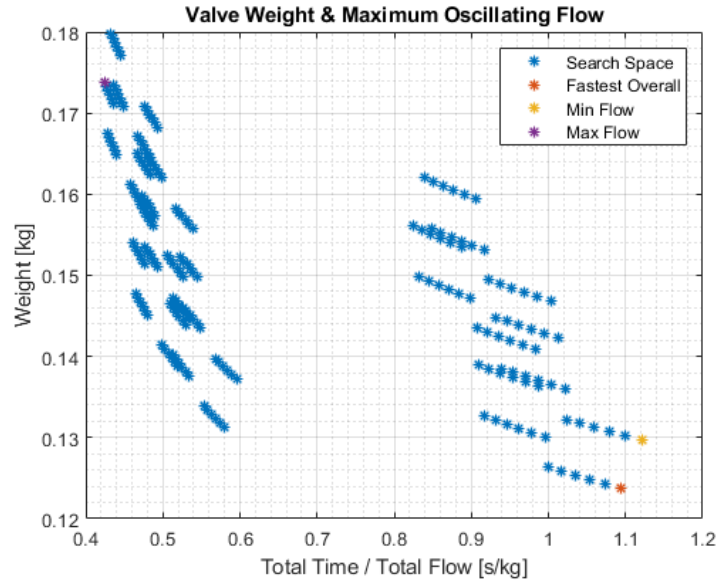


Figure 6.6: x axis represents the time it takes to flow 1 kg of gas during an oscillating valve operation (continuous opening and closing of the valve).

tural elements these were as follows:

$$c_a = 0.05 : 0.02 : 0.09 \text{ mm}$$

$$c_r = 0.05 : 0.02 : 0.09 \text{ mm}$$

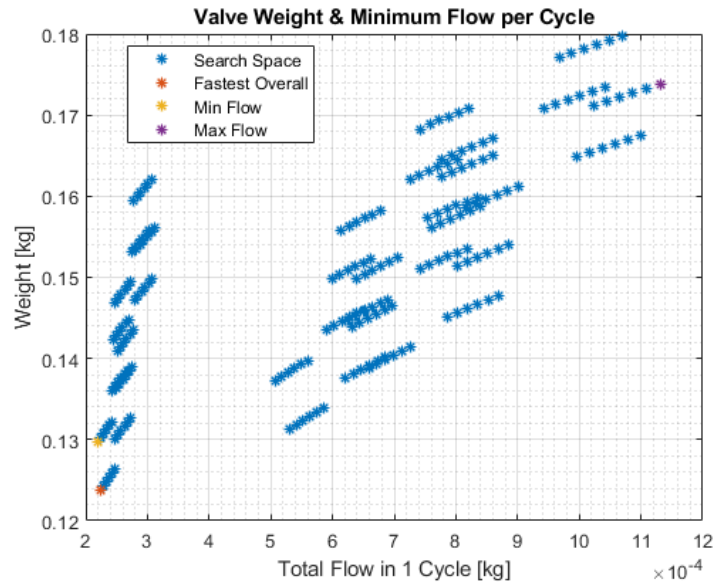


Figure 6.7: Results of simulation: Valve Weight and minimum flow per cycle

A total of 9 designs were simulated.

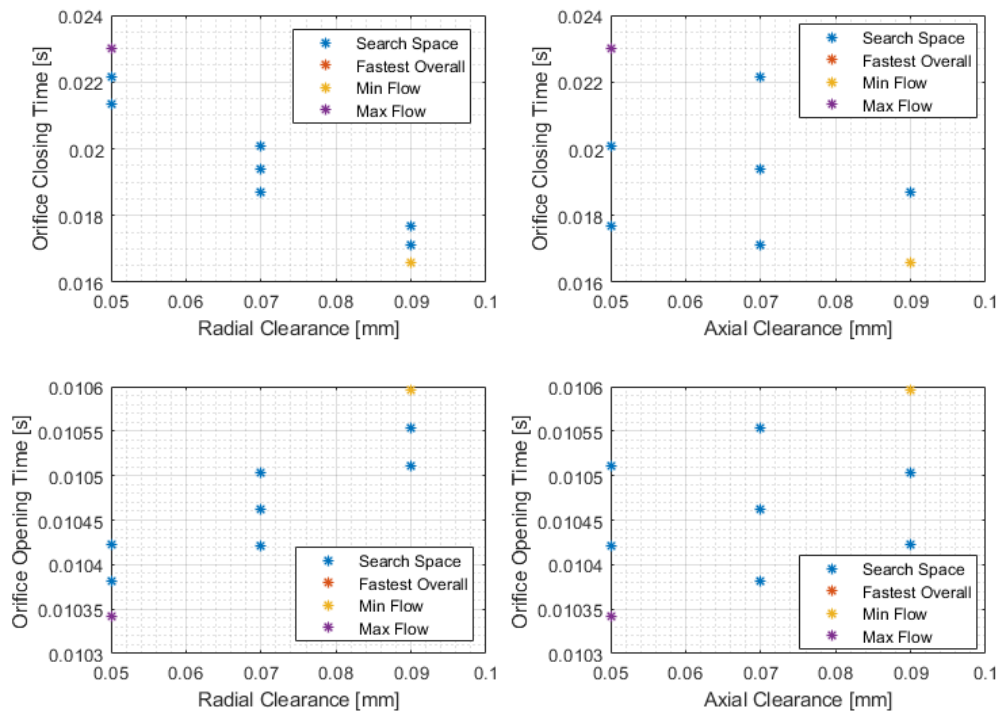


Figure 6.8: The effect of clearances on valve opening and closing times.

As seen in fig. 6.8, radial and axial clearance is directly proportional with orifice opening time and inversely proportional with orifice closing time. It should be noted though the radial clearance has a much higher impact than the axial clearance. This is because as radial clearance increases the armature surface area decreases and the coil turns decreases.

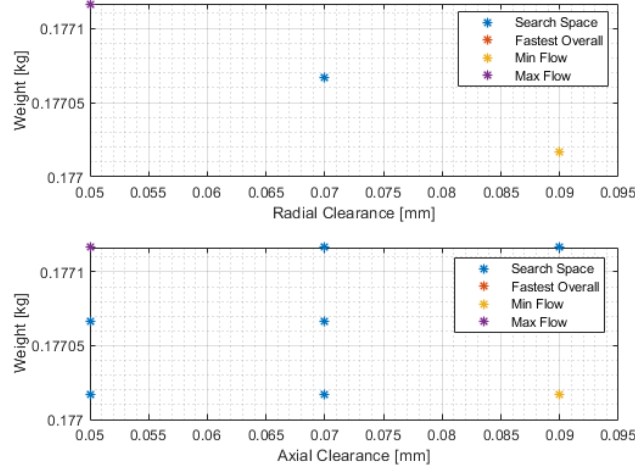


Figure 6.9: The effect of clearances on valve weight.

While axial clearance has almost no effect on weight, radial clearance has a minimal effect due to reduced number of turns and reduced armature surface area.

The final design is presented in fig. 6.10. Final design can be compared with the initial design of reference in fig. 3.1. Notice that the optimization was only done on magnetic circuit elements. The structural casing, valve seat and seal was omitted for the computation because it is assumed that the smaller solenoid and magnetic circuit design will lead to the smallest overall design. With the addition of valve seat, casing and seal the resulting valve should not exceed 200g in weight.

6.5 Sensitivity Analysis

The results of the sensitivity analysis on structural parameters are shown in table 6.1. This analysis is performed by numerically differentiating with a step of $0.02E-3mm$ for the parameters that are in meters. For dimensionless parameters PR and μ_r step

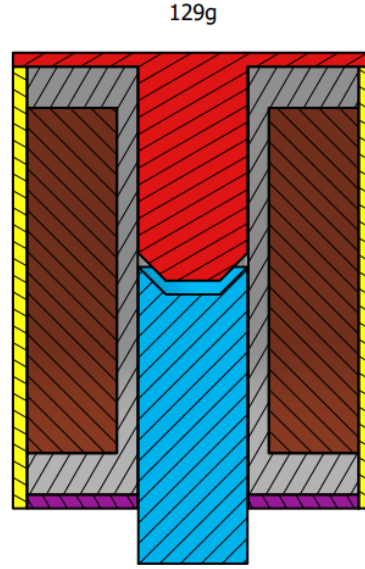


Figure 6.10: The 3D model of the optimized valve.

size was picked as 0.01 and 1 respectively.

Radial clearance, c_r , has the highest impact on $\tau_{opening}$ and $\tau_{closing}$. First, as the radial clearance increases effective surface area of armature decreases. Second, as the radial clearance increases the number of coil turns decreases. Both of these effects reduce inductance thus, resulting in a slower $\tau_{opening}$ and faster $\tau_{closing}$. Since the total flow per cycle is directly dependent on $\tau_{closing}$, c_r also has the highest impact on it. Total power used for a cycle is also directly proportional to inductance, thus c_r dominates total power used in a cycle.

Coil outer radius, r_{Cout} , has the highest impact on the valve weight because the densest material used in the valve is the copper wire. As the r_{Cout} increases the copper wire weight, cylinder surface area, increases by its square.

$$r_{Cout}^2 \sim weight \quad (6.1)$$

Table 6.1: Sensitivity Matrix

| | $\tau_{opening}$ [s] | $\tau_{closing}$ [s] | Flow [kg] | Power [W] | Weight [kg] |
|-----------------|----------------------|----------------------|-----------|-----------|-------------|
| c_r [m] | 6.97E+01 | -6.97E+01 | -1.00E+01 | -1.64E+03 | -7.28E+00 |
| c_a [m] | 3.05E+00 | -3.05E+00 | -1.49E+00 | -2.45E+02 | 0.00E+00 |
| h_C [m] | -3.50E-01 | 3.50E-01 | 1.36E-02 | 6.83E+00 | 4.98E+00 |
| r_{Cout} [m] | -2.20E+00 | 2.20E+00 | 1.69E-01 | 5.31E+01 | 2.18E+01 |
| D_w [m] | 5.00E-02 | -5.00E-02 | 1.55E-03 | 3.42E-01 | 0.00E+00 |
| t_{cfr} [m] | 8.00E-01 | -8.00E-01 | -2.15E-01 | -5.12E+01 | -5.41E+00 |
| t_{cfa} [m] | 1.00E-01 | -1.00E-01 | -1.07E-02 | -1.70E+00 | 2.94E+00 |
| t_{mba} [m] | -4.45E+00 | 4.45E+00 | 6.46E-01 | 1.04E+02 | 4.42E+00 |
| t_{mta} [m] | -6.50E-01 | 6.50E-01 | 9.54E-02 | 1.55E+01 | 3.15E+00 |
| r_A [m] | 4.00E+00 | -4.00E+00 | -1.29E-01 | -2.21E+01 | -1.87E+00 |
| r_{cham} [m] | 9.50E-01 | -9.50E-01 | -7.70E-02 | -4.75E+00 | 0.00E+00 |
| h_{cham} [m] | -1.40E+00 | 1.40E+00 | 1.15E-01 | 6.96E+00 | 0.00E+00 |
| t_{shell} [m] | -2.50E-01 | 2.50E-01 | 3.46E-02 | 5.58E+00 | 1.78E+01 |
| PR | -9.55E-03 | 9.55E-03 | 1.19E-03 | 3.29E-01 | 8.00E-02 |
| h_{air} [m] | 3.06E+01 | -3.06E+01 | -2.14E-01 | -1.46E+00 | 0.00E+00 |
| μ_r | -5.00E-06 | 5.00E-06 | 7.16E-07 | 1.14E-04 | 0.00E+00 |

6.6 \dot{m} vs ΔP Performance

The fig. 6.11 shows the pressure drop across the valve for different flow rates in 50 Bar inlet pressure and 273K temperature for nitrogen gas. ΔP is plotted until the maximum flow rate limit under these conditions. It should be noted that this result is obtained by assuming perfect pressure recovery working fluid after passing through each orifice.

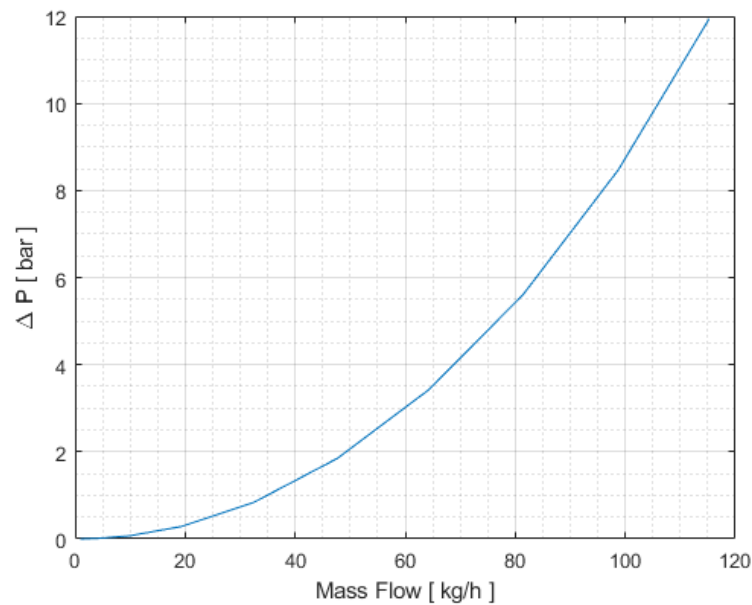


Figure 6.11: \dot{m} vs ΔP for 50 bar inlet pressure and 273K temperature for nitrogen gas.

Chapter 7

CONCLUSION

Our multi-physics simulation for a solenoid valve reinforces our hypothesis that the reaction time of solenoid valve are driven by the electromagnetism. In order to design an efficient fast response solenoid valve one must thoroughly analyze the effects of each structural element and optimize each for the given objective.

For a fast normally closed solenoid valve, we desire to have the highest inductance when it is powered off and the lowest inductance when it is open state. Unfortunately this is the opposite of how solenoid valves work. Solenoid valve have the lowest inductance due to the air gap's dominating magnetic reluctance when closed. As the armature retracts this air gap reluctance diminishes and we are left with the highest reluctance for our solenoid. Thus, there is a trade-off between fast opening and closing. To improve valve response times, more complex electrical circuits can be designed [Zhao et al., 2017b]. The optimization model developed in this study could be improved by adding boost voltage for the opening phase and a reverse voltage for the closing phase in the future. These electrical modifications for the valve circuit will come with a reliability and complexity cost but it should not be hard to implement.

As seen in the sensitivity analysis, manufacturing tolerances and clearance have high impact on performance parameters. This multi-physics model can be improved by taking the viscous effects in the tight clearances in to account. Sharp edges on the armature and the chamfer design should be picked carefully due to magnetic flux concentration. In our physical prototypes we observed that these sharp edges causes magnetic flux saturation and this hampers the total magneto motive force generated by the solenoid.

BIBLIOGRAPHY

- [Choi et al., 2021] Choi, J., Ahn, J., and Kim, H. (2021). Modeling the dynamic behavior of a pilot-operated solenoid valve for an ultra-high pressure vessel. *Applied Sciences*, 11:2329.
- [Inst, 2019] Inst (2019). How pilot operated solenoid valve works.
- [NASA, 2021] NASA (2021). Isentropic flow equations.
- [OpenStax, 2022] OpenStax (2022). 23.1: Rl circuits. *Physics LibreTexts*.
- [Schimpf, 2013] Schimpf, P. (2013). A detailed explanation of solenoid force. *International Journal on Recent Trends in Engineering & Technology (IJRTET)*, 8:7–14.
- [Yang et al., 2019] Yang, M., Zhang, J., Bing, X., and Wang, W. (2019). Study on electromagnetic force of the new micro digital valve. *Microsystem Technologies*, 25.
- [Zhao et al., 2017a] Zhao, J., Shi, Y., Grekhov, L., and Ma, X. (2017a). Effects of structure parameters on the static electromagnetic characteristics of high speed solenoid valves. *International Journal of Applied Electromagnetics and Mechanics*, 55:1–16.
- [Zhao et al., 2017b] Zhao, J., Wang, M., Wang, Z., Grekhov, L., Qiu, T., and Ma, X. (2017b). Different boost voltage effects on the dynamic response and energy losses of high-speed solenoid valves. *Applied Thermal Engineering*, 123:1494–1503.

Appendix A

Source code: <https://github.com/khanliKU/thesis>